Application of Meshfree Methods to Numerically Simulate Microscale Deformations of Different Plant Food Materials during Drying

H. C. P. Karunasena[a,b], R. J. Brown[a], Y. T. Gu[a] and W. Senadeera[a,*]

[a] School of Chemistry Physics and Mechanical Engineering, Faculty of Science and Engineering, Queensland University of Technology, 2 George Street, Brisbane, QLD 4001, Australia.
[b] Department of Mechanical and Manufacturing Engineering, Faculty of Engineering, University of Ruhuna, Hapugala, Galle, Sri Lanka.

Abstract

Plant food materials have a very high demand in the consumer market and therefore, improved food products and efficient processing techniques are concurrently being researched in food engineering. In this context, numerical modelling and simulation techniques have a very high potential to reveal fundamentals of the underlying mechanisms involved. However, numerical modelling of plant food materials during drying becomes quite challenging, mainly due to the complexity of the multiphase microstructure of the material, which undergoes excessive deformations during drying. In this regard, conventional grid-based modelling techniques have particularly limited applicability due to their inflexible grid-based fundamental limitations. As a result meshfree methods have recently been developed which offer a more adaptable approach to problem domains of this nature, due to the fundamental grid-free advantages. In this work, a previously developed meshfree based two-dimensional plant tissue model is used for a comparative study of microscale morphological changes of several food materials during drying. The model involves Smoothed Particle Hydrodynamics (SPH) and Discrete Element Method (DEM) to represent fluid and solid phases of the cellular structure. Simulation are conducted on apple, potato, carrot and grape tissues and the results are qualitatively and quantitatively compared and related with experimental findings obtained from the literature. The study revealed that cellular deformations are highly sensitive to cell dimensions, cell wall physical and mechanical properties, middle lamella properties and turgor pressure. In particular, the meshfree model is well capable of simulating critically dried tissues at lower moisture content and turgor pressure, which lead to cell wall wrinkling. The findings further highlighted the potential applicability of the meshfree approach to model large deformations of the plant tissue microstructure during drying, providing a distinct advantage over the state of the art grid-based microscale drying models.

Keywords: Food drying, Dehydration; Shrinkage; Plant tissues; Microscale models; Meshfree methods; Numerical modelling; SPH; DEM;

∗ Corresponding author. Address: School of Chemistry Physics and Mechanical Engineering, Faculty of Science and Engineering, Queensland University of Technology, GPO Box 2434, Brisbane, QLD 4001, Australia.
Tel.:+61-7-3138 6887; Fax: +61-7-3138 1516; E-mail: w3.senadeera@qut.edu.au

1. Introduction

In the global food market, plant based food materials hold a significant proportion, and numerous researches are being conducted to improve new food products and efficient processing techniques. In this context, food drying is used to process about 20% of the world's perishable crops and is therefore can be considered as one of the key plant food processing techniques (Grabowski et al., 2003). Since plant food materials usually contain very high moisture, even up to 90% by weight (Jangam, 2011), are highly subjected to spoilage. Therefore, food drying can be used as a preservation technique since it principally reduces moisture from the plant material structure. With the objective of improving such food drying processes, different drying techniques have evolved (Martin et al., 2006). All these processing techniques cause the food material to undergo structural deformations and other changes of the physical or chemical properties. These alterations eventually result in microscale and macroscale changes of the food structure such as shrinkage, which is one of the most important concerns in food processing. Shrinkage is mainly governed by the moisture content of the food material (Hills and Remigereau, 1997; Karunasena et al., 2014a; Lee et al., 1967; Lewicki and Drzewucka, 1998; Lewicki and Pawlak, 2003; Lozano et al., 1980; Mayor et al., 2005; Ramos et al., 2004), drying temperature (Bai et al., 2002; Funebo et al., 2000; Karunasena et al., 2014a; Rahman et al., 2005) and cell turgor pressure (Bartlett et al., 2012). Such structural deformations are present in both microscale and macroscale of the food structure and they are well interrelated (Han et al., 2010; Hills and Remigereau, 1997; Lee et al., 1967; Lewicki and Drzewucka, 1998; Mayor et al., 2005; Ramos et al., 2004; Sabarez et al., 2012; Witrowa-Rajchert and Rząca, 2009). In order to understand the driving factors of these deformations, researchers have extensively focused on different empirical models (Mayor and Sereno, 2004) and theoretical models (Crapiste et al., 1988-a; Zhu and Melrose, 2003).

However, limited research has been conducted on numerical modelling of the structural deformations, both in the macroscale and microscale. The available numerical models are mostly based on grid-based modelling techniques such as Finite Element Methods (FEM) and Finite Difference Methods (FDM), which have limited capability to model multiphase non-continuum materials under large deformation and phase change conditions (Liu and Liu, 2003). For instance, in the case of macroscale models, a gel material model based on FEM is reported which is capable of simulating dried plant leaves (Liu et al., 2010). The key limitation here is the hypothetical gel material assumption, which approximates the plant material to a continuum, which is fundamentally not realistic. Also, when modelling different plant materials, it becomes quite challenging to estimate the appropriate hypothetical gel material properties corresponding to the drying conditions of different plant materials. Also, in their work, they have not demonstrated any means of directly relating the moisture content reduction with the shrinkage, which is another critical shortcoming when it comes to industrial drying applications. Another FEM based plant leaf drying model is reported, which accounts for surface wrinkling of plant leaves during drying (Jeong et al., 2013). The work has replicated actual wrinkles of leaves at different moisture contents and even can account for localised variations of the moisture content. However, their two-

layer thin structure-based model has clear limitations when modelling actual 3-D plant material structures, because the two-layer approximation becomes invalid.

Next, in the case of microscale models, there are several studies reported which are mainly dedicated to micromechanical studies of the fresh cells and tissues, rather than drying (Gao and Pitt, 1991; Honda et al., 2004; Rudge and Haseloff, 2005; Wang et al., 2004; Wu and Pitts, 1999; Zhu and Melrose, 2003). When it comes to microscale drying models in particular, a very recent work is reported on pear tissue drying, which is also based on FEM, and couples water transport phenomena with cell deformations (Fanta et al., 2014). Although the model has demonstrated some level of capability to model cellular shrinkage, it can only simulate a limited moisture content range (dry basis normalized moisture content reduction limited to 30%). Since the moisture content reduction is usually greater than 90% in actual drying processes, this model can be considered as valid only for the initial stage of a given drying process. Also, another key limitation is its inability to account for cell wall wrinkling, which is critical when replicating actual cell wall deformations. This limitation is due to the vertex model involved in the model, which generates the cellular structure as a set of polygon-shaped cells with linear sides. Adjacent cells share the same sides and during drying, these polygons are allowed to undergo deformations, but the linearity of the sides is maintained unaltered during drying, which is not realistic. These shortcomings highlight the fundamental limitations of the grid-based approaches when used in challenging problem domains such as cellular structural deformations during drying, which involves excessive deformations of multiphase non-continuum materials.

The research gap identified by the above brief literature review can be filled by recently developed meshfree methods, which offer a more adaptable approach to these problem domains. Since the meshfree modelling approaches fundamentally do not involve a grid to discretise the problem domain, those do not suffer from grid-based limitations such as in the case of FEM or FDM (Frank and Perré, 2010; Liu and Liu, 2003). Therefore, such novel numerical techniques have the potential to handle the complex deformation characteristics of plant materials by accurately accounting for the inherited properties of the cellular structure. In this regard, we focused on microstructural models, since those can better represent fundamental mechanisms, which eventually drive the macroscale deformations of the food material. Accordingly, meshfree-based 2-D plant cell and tissue models were initially developed (Karunasena et al., 2014c, 2014e; Karunasena et al., 2014b, 2014d). There, the cell fluid is modelled with Smoothed Particle Hydrodynamics (SPH), which is a popular particle-based meshfree method (Gingold and Monaghan, 1977; Liu and Liu, 2003). SPH is frequently used to study hydrodynamic problems and the technique involves a set of non-interconnected particles to discretise a given problem domain. These particles are initialized with physical properties corresponding to the initial state of the problem domain and allowed to evolve with time. Also, the particles can move in space in order to represent material deformations. The technique is also highly adaptive to incorporate novel physical phenomena on to the underlying basic formulations of the method, which is an added advantage when it comes to novel developments (Liu and Liu, 2003). For the above cell and tissue models, SPH is coupled with Discrete Element Method (DEM), which is used to model the solid dominated cell wall structure (Liedekerke et al., 2010; Van Liedekerke et al., 2011).

Using this coupled SPH-DEM approach, a two-dimensional (2-D) single cell drying model was initially developed and drying simulations were conducted apple cells by varying the cellular moisture content and the turgor pressure (Karunasena et al., 2014b). Next, by considering the cell perimeter contractions observed from experiments (Karunasena et al., 2014a; Mayor et al., 2005), the model was further improved to account for cell wall contraction forces, cell wall drying effects and turgor pressure variations (Karunasena et al., 2014c). Based on this particular 2-D single cell drying model, a basic tissue drying model was firstly developed by using rectangular cells, with a primary brick-like cell arrangement (Karunasena et al., 2014d). In order to further improve the intercellular contacts, hexagonal cells were used, leading to a more realistic honeycomb tissue structure observed in real plant materials (Karunasena et al., 2014e). The model predictions were in favourably good agreement with cellular deformations observed from convective drying experiments on apples, both qualitatively and quantitatively (Karunasena et al., 2014a; Mayor et al., 2005). Further, when compared to the state of the art grid-based microscale tissue drying models (Fanta et al., 2014), the new meshfree-based model was advantageous particularly in terms of the amount of moisture reduction (70% achieved) and the capability of accounting for cell wall wrinkling during drying.

In this background, this work uses the same previous tissue model (Karunasena et al., 2014e), in order to numerically study the difference of morphological changes of four distinct plant food materials as affected by differences in the cellular structural properties such as: cell size, wall thickness, cell wall stiffness, cell wall contractions during drying, turgor pressure, and pectin layer dimensions and stiffness. The four food materials (apple, potato, carrot and grapes) were selected by considering their popularity in the food processing industry, and the availability of experimental results from the literature for comparison and validation of the simulation results. It is further aimed to highlight the flexibility of the meshfree-based approach for modelling different plant microstructures. When compared with the state of the art, this work is potentially the very first meshfree-based numerical analysis, simultaneously applied on several plant food materials to study their unique characteristics of microscale morphological changes during drying.

The paper is organized such that the basic concepts used for the cell model are firstly introduced. Since this work is a continuation of some previous works, details corresponding to model formulations are mainly included in Appendix A. Experimental findings from literature which were used for comparison and validation of the models are presented next. Thereafter, single cell and tissue based results are presented and compared for relative differences. Further, experimental findings obtained from literature are used to compare the model predictions both qualitatively and quantitatively. Finally, key insights drawn from the study along with prospective future improvements are discussed.

2. Model development

2.1. Modelling concepts used

As detailed out in our previous works (Karunasena et al., 2014c; 2014e), the 2-D model used in this work approximates a plant tissue as a single layer of aggregated cells which resemble fluid filled cylinders with solid boundaries (see Fig. 1(a)). Now, as shown in Fig. 1(b), the top surface of any cell is considered as a 2-D model which can represent the mechanisms of the whole cell. In the cell model, the fluid and the wall are treated separately as shown in Fig. 1(b) and (c), where the fluid-dominated cell fluid is modelled with SPH and the solid-dominated cell wall is modelled with DEM. As shown in Fig. 1(c), both SPH and DEM models use particles to discretise the domains and the related governing equations were defined on these particles.

In the case of the cell wall, the DEM model is setup such that the discretised elements of the cell wall are represented by individual particles as shown in Fig. 1(d). The wall model approximates the cell wall material to a visco-elastic solid, and a Neo-Hookean solid material approximation is used along with a supplementary viscous term (Liedekerke et al., 2010). Additionally, several new force interactions were introduced in previous works in order to account for drying related physical changes and to improve the model performance (Karunasena et al., 2014c; Karunasena et al., 2014b). Accordingly, as presented in Fig. 2, the cell wall model used in this work involves a set of distinct force interactions: cell wall stiff forces ($\boldsymbol{F}^{e}$), wall damping forces ($\boldsymbol{F}^{d}$), wall-fluid repulsion forces ($\boldsymbol{F}^{rf}$), non-bonded wall-wall repulsion forces ($\boldsymbol{F}^{rw}$), wall-fluid attraction forces ($\boldsymbol{F}^{a}$), forces due to bending stiffness of the cell wall ($\boldsymbol{F}^{b}$), and forces to produce contractions of the cell wall during drying ($\boldsymbol{F}^{c}$). In the case of the cell fluid, it is approximated to a Newtonian fluid with low Reynolds number flow characteristics, and modelled using SPH, along with additional force interactions to account for fluid-wall boundary conditions. Accordingly as show in Fig. 3, the fluid model involves four distinct force interactions: fluid pressure forces ($\boldsymbol{F}^{p}$), fluid viscous forces ($\boldsymbol{F}^{v}$), wall-fluid repulsion forces ($\boldsymbol{F}^{rw}$) and wall-fluid attraction forces ($\boldsymbol{F}^{a}$). (see Section 6.1 – 6.2 under Appendix A for detailed formulations of the cell wall and fluid models)

Then such single cells are aggregated to from a simplified tissue model as shown in Fig. 4(a) and (b), by using a hexagonal initial cell shape, in order to replicate honeycomb cell shapes frequently observed in real tissues (Karunasena et al., 2014e). This cellular structure accommodates spaces between adjacent cell walls, replicating middle lamella (pectin layer) in real tissues. Accordingly, as presented in Fig. 4(c) and (d), the cell-cell interactions are simply defined using two force interactions: pectin layer stiff forces $\boldsymbol{F}_{km}^{e\_pectin}$ and cell-cell repulsion forces $\boldsymbol{F}_{km}^{rc}$ (see Section 6.3 under Appendix A for details). With this cell arrangement, a rectangular shaped tissue is developed by aggregating 23 cells, and sections below describe how the model is setup in order to simulate drying related deformations, and how the model is customized for different plant food materials.

2.2. Setting up the particle scheme for each cell in the tissue

Firstly, each plant food material was modelled by using customized model parameters obtained from microscopic experimental findings and other numerical models available in literature (see Section 3 for details). Accordingly, each of the single cells in the tissue was setup by uniformly distributing the wall particles on a hexagonal wall boundary. Then, the fluid particles were placed in the cell interior by using a square grid

arrangement such that the gap between fluid particles is equal to the inter-particle spacing of the cell wall. After a series of trial simulations, 96 wall particles were selected for the cell wall and the corresponding cell fluid particle number was 656 (Karunasena et al., 2014e). The model is time-evolved using a Leapfrog integrator (Liu and Liu, 2003) with a time step defined by the Courant-Friedrichs-Lewy (CFL) criteria (Colagrossi et al., 2012; Liu and Liu, 2003). Further, in order to ensure the stability of the model, fluid particle penetrations through the cell wall is avoided by using a set of virtual particles that were placed in between cell wall particles (Karunasena et al., 2014b; Liedekerke et al., 2010).

2.3. Simulation of fresh single cell

In order to simulate fresh cells, Eq. (A.18) was used (see Section 6.2 under Appendix A). Accordingly, the model allows moisture transfer through the semi-permeable cell wall, whenever the cell turgor pressure and the magnitude of the osmotic potential are different, replicating real cells. As a result of such fluid mass fluctuations, cell fluid density varies according to Eq. (A.14), causing significant turgor pressure fluctuations as defined by Eq. (A.13). Such turgor pressure fluctuations tend to displace the cell wall, causing cellular dimensional changes. Such changes result in secondary turgor pressure fluctuations, which eventually cause cell fluid mass fluctuations as defined in Eq. (A.18). After a number of similar time evolutions, the effective mass transfer across the cell wall reduces considerably and the model reaches a steady state condition where the cell fluid turgor pressure becomes approximately equal to the magnitude of the initially set osmotic potential. Corresponding to each material type, this particular steady state particle arrangement and related physical properties are used to represent fresh cell states. Since higher turgor pressure values are used for fresh cell simulations (see Section 3), the cell shapes tend to resemble turgid real cells owning higher moisture contents and turgor pressures.

2.4. Simulation of dried single cell

In the case of dried cells, a moisture-content-domain simulation method was used in order to avoid excessive computational overhead, when simulating each dryness state separately (Karunasena et al., 2014b). Further, cell fluid moisture content reduction, turgor pressure reduction and cell wall drying effects were also involved, which were introduced previously (Karunasena et al., 2014c). Accordingly, it was hypothesised that the cell turgor pressure would remain positive during drying and will gradually reduce with the reduction of the cell moisture content. For instance, in the case where 200 kPa is selected as the fresh cell turgor pressure (see Table 1 and Table 2 for the actual values used for each material), the dried cells of: X/X_0 = 0.8, X/X_0 = 0.6, X/X_0 = 0.4 and X/X_0 = 0.25 were simulated with initial turgor pressures of 160 kPa, 120 kPa, 80 kPa and 50 kPa. In order to ensure the model stability in these desired turgor pressure values, the magnitudes of the osmotic potential corresponding to each dryness state are set equal to the corresponding turgor pressure, and are kept constant during time evolution. Further, cell wall drying is also accounted for by setting the initial cell wall mass proportional to the X/X_0 of the cell in each case, and is not evolved with time. When the model reaches steady state condition at the end of each time evolution, the corresponding particle arrangement and related physical properties are used to represent the corresponding dried cell states of the particular plant food material.

2.5. Simulation of tissues

The above mentioned single cell models were aggregated to form rectangular tissues, following a method proposed previously (Karunasena et al., 2014e). The method uses the above mentioned honeycomb-shaped tissue structure with a positive pectin layer gap, and also incorporates improved cell-cell interactions compared to the state of the art SPH-DEM based plant cell models (Liedekerke et al., 2010) (see Section 6.1 – 6.3 under Appendix A for details). Further, in these simulations, all the cells across the whole tissue are set to undergo similar moisture content and turgor pressure reductions (i.e. all the cells in the tissue follow a similar dying process and won similar dryness statutes simultaneously). However, in actual drying processes when larger tissues with a higher number of cells are involved, and such tissues are subjected to rapid drying processes like forced convective drying, the tissues are usually subject to case hardening effects where the outermost cell layers get extensively dried compared to internal cells. In this work, such finer effects are not focused upon since our main objective is to study the cell morphological changes as affected by cellular variability. However, the proposed modelling approach is fundamentally capable of handling such effects also. For instance, one can set unique moisture content and turgor pressure values for different cell layers in the tissue, and time evolve them with minimum difficulty.

At the end of each time evolution, when these tissues (fresh or dried) reach steady state conditions, the dry basis moisture content X (= kg $_{\text{water}}$ / kg $_{\text{dry material}}$) are computed and related with a set of average cellular geometrical parameters: cell area (A), feret diameter[1] (D), perimeter (P), roundness[2] (R), elongation[3] (EL) and compactness[4] (C), in order to characterise different tissue dryness states. Eventually, normalized parameters (X/X_0, A/A_0, D/D_0, P/P_0, R/R_0, EL/EL_0 and C/C_0) are used in order to facilitate easy comparison of the results. These findings on the four plant food materials are firstly compared for relative differences, and then related with the corresponding experimental findings obtained from the literature (see Section 3 for details).

2.6. Computer implementation of the model and computational accuracy

The above mentioned model formulations were programmed in a parallel C++ code and a High Performance Computer (HPC) was used to run the simulations. Algorithms available in an existing FORTRAN based SPH source code (Liu and Liu, 2003) were partly referred when developing the C++ source code, and the Open Visualization Tool (OVITO) (Stukowski, 2010) was used to perform model visualizations. In order to evaluate the numerical accuracy of the model used, the model consistency error was estimated according to the method presented previously (Karunasena et al., 2014b), and the selected particle scheme only produced model consistency errors within 3% and density fluctuations within 0.1%. When compared with the state of the art

[1] $\sqrt{4A/\pi}$
[2] $4\pi A/P^2$
[3] $\sqrt{4A/\pi}$ /(major axis length)
[4] major axis length/minor axis length

SPH-DEM pant cell models reported in literature (Liedekerke et al., 2010), these findings compare favourably, and therefore the numerical accuracy of this model is assured.

3. Experimental literature data used for model development and validation

The key physical properties used to model the above four plant food materials are summarized in Table 1. Some properties were directly adopted from literature and some others were calculated or assumed. For instance, the initial heights of the cylindrical cells were determined by assuming that the actual cells in tissues are spheres with initial cell diameter found from literature, and equating the volume of a cylindrical cell model to the volume of actual spherical cells. The pectin layer thickness was set such that it is proportional to the cell size and its stiffness was set by following several trial simulations in order to have comparable initial cell shapes and cell-cell contacts in all the four plant food materials used. For grape and carrot, the cell wall shear modulus was set such that the Young's modulus (E) is 100 MPa, which would produce comparable cell wall stiffness magnitudes at corresponding cell wall thickness values. Due to the absence of distinct literature data, the turgor pressure of grapes and potatoes were set equal to that of apples. The osmotic potential was set such that its magnitude is equal to the initial turgor pressure in each case, as discussed in Section 2.4. Other model parameters commonly applied for all the food materials are listed in Table 2 with corresponding sources.

Additionally, in order to compare and validate the model predictions both qualitatively and quantitatively, another set of literature findings were used. For qualitative data, microscopic images of fresh and dried plant tissues were used. For quantitative data, the geometrical parameters specified in Section 2.2 were referred to, depending on the availability of literature data. Using these findings, model predictions were compared and validated. Table 3 shows the corresponding literature findings used for model validation (See Section 4.2 for details of microscopy images and geometrical parameters used for each plant food material).

4. Results and discussion

4.1. Comparative overall differences of single cell and tissue morphological changes during drying

Using the modelling concepts described in Section 2 and the physical properties presented in Section 3, tissues of the selected plant food materials were simulated for different dryness states. Fig. 5 presents single cell simulation results and Fig. 6 presents tissue results. In both figures, all images are scaled in order to highlight the relative differences of morphological characteristics. Firstly, it is evident from Fig. 5 that the apple cells and grape cells are similar in size and are comparatively smaller to the potato cells. The carrot cells are the smallest. When comparing with the initial hexagonal cell shape, it is clearly observed that the fresh cells in each material type have inflated. When considering the dried cells, the general observation is that their dimensions have reduced, resembling the frequently observed cellular shrinkage during drying. As seen from Fig. 5(b) - (f), the carrot cells experience an intense shrinkage behaviour which is due to the higher value of the parameter a used in the cell wall contraction force field (see Table 1). In contrast, the potato cells undergo limited shrinkage (see

Fig. 5(b) and (f) on potato cells), compared to the other three materials, which is mainly due to the lower value of the parameter a used. However, the single cells are fairly circular and are independent of the dryness state and the material type (see Fig. 5 (b) to (f) on all materials). This is mainly due to the positive turgor pressure involved and the absence of the intercellular interactions in these single cell models.

Fig. 6 presents tissue simulation results and the relative size difference of the tissues is clearly observed, which is basically due to the cell size difference as discussed above. Also, the fresh and dried cells in each tissue commonly have a basic hexagonal shape, resembling the frequently observed honeycomb tissue structure of plant materials. This is mainly due to the intercellular interactions, which are not involved in the single cell simulations mentioned above. Next, when considering the apple and grape tissues, although similar initial cell and tissue geometries are used for modelling (see Table 1), the dried tissues shapes indicate a significant difference. Compared to the fresh tissue size, dried tissues of grape have experienced a higher shrinkage than apple tissues, which is even evident by comparing the centre-most cell of both the tissues. It is mainly due to the influence of cell wall contraction force fields. When referring to Table 1, the cell wall contraction effect of grape is comparatively stronger than apple cells. The intense cell wall contraction effect of grapes can be seen in the single cell simulation results also (see dried cells of apple and grape in Fig. 5). Further, one can relate this to the differences in cell wall thickness and the stiffness. However, it should be noted here that according to the cell wall stiff force formula used in the DEM model as presented in Eqn. (A.2), the cell wall stiffness is mainly influenced by the product of the Young's modulus of the cell wall material and the cell wall thickness (T_0). In this regard, when the corresponding E and T_0 values are referred to in Table 1, the values of apple and grape cell walls indicate a fairly similar stiff behaviour (their $E \times T_0$ products are quite similar). So, it implies that this intense shrinkage behaviour of grape tissue compared to apple tissue, is mainly due to the differences of the cell wall contraction effects during drying. Further, when the bulk level tissue geometries are considered (with reference to the tissue boundaries), the apple tissues shrink towards the centre of each tissue, compared to the grape tissues, and it is mainly due to the differences of cell wall contraction forces. When considering the potato tissue, due to its lager cell size, the tissues are comparatively larger than apple, grape or carrot tissues. Also, as mentioned above, since the cell wall contracting effects are weaker in the potato cells, compared to other tissue types (lower value for parameter a in Table 1), the potato tissues undergo only a limited shrinkage. Accordingly, even the extremely dried potato cells retain fairly hexagonal shapes, so as the original rectangular shape of the tissue (considering the outer boundaries of the tissue). These findings imply that the tissue shrinkage is highly influenced by the cell wall contraction forces, the cell wall stiffness and the cell size.

When considering the carrot tissue, as presented in Fig. 6, it owns the smallest size compared to all other tissues studied in this work, which is basically due to the smaller cell size involved (see Table 1). Also, as observed in apple and grape tissues, the carrot tissues also undergo extensive shrinkage, which is due to the higher values of the cell wall contraction force parameters. In addition, compared to the other three tissues, dried carrot tissues own a quite different shape, which resembles an inflated square. This is mainly due to the comparatively higher turgor pressure used in modelling carrot cells (see Table 1). These findings imply that the tissue shrinkage is also influenced by the cell turgor pressure. Sections below further elaborate these localized differences of each

plant food material type by further comparing with the experimental findings, both qualitatively and quantitatively.

4.2. Detailed analysis of morphological changes of apple tissues during drying

Firstly as can be seen from Fig. 7, the SEM images of apple tissues obtained from experiments (Karunasena et al., 2014a), indicate that both the fresh cells and dried cells in real tissues are closely-packed, and particularly the cells in dried tissues have undergone significant shrinkage along with cell wall wrinkling. Also, the fresh cells are comparatively circular compared to the dried cells, which is due to the higher turgor pressures existing in the fresh cells. Fig. 8 presents the simulated apple tissues and Fig. 9 presents the enlarged centre-most region of the tissues. When comparing the initial condition and the fresh cell condition (Fig. 8(a) and Fig. 9(a)), it is clearly observed that the cells in the fresh tissue have inflated and increased their size. The cells in the fresh tissue are fairly circular, which is mainly due to the higher turgor pressure involved, which is in favourable agreement with the experimental findings. Also, it is observed from dried tissues that the basic hexagonal cell shape is further maintained even at dried conditions, replicating a closely-packed honeycomb tissue structure frequently observed in pant tissues. Further, when comparing with the fresh tissue, the dried tissues have clearly experienced shrinkage and have undergone dimensional contractions both locally at cell level and globally in tissue level. From Fig. 8, it is observed that the local cell shapes, particularly in dried tissues states are quite different at different cell layers in the tissue, which is due to the differences of intercellular contacts. In this regard, cells in actual dried tissues can undergo such shape changes due to the localized difference of the cell moisture content, which can lead to the well-known case hardening phenomenon. Although, numerical modelling of such complicated realistic tissue states are technically viable using the proposed meshfree approach, such studies were not conduced in this work, since the main focus here is to study the relative difference between different food material structures during drying.

As mentioned above, the SEM images of apple cells clearly indicate cell wall wrinkling behaviour, particularly at dried conditions. It is interesting to observe that the tissue model has also demonstrated the capability to replicate cell wall wrinkling effects in dried tissues (see Fig. 9(e) and (f)). In order to elaborate these effects further, the geometrical parameters introduced in Section 2.5 were quantified for different tissue states and are presented in Fig. 10, along with corresponding experimental results. Also, single cell simulation results are used in order to highlight the additional capabilities of the tissue model which incorporate intercellular interactions. It should be noted here that, only the centre most 7 cells were used for these cellular geometrical parameter calculations and the outer most cell layers were not considered in order to sufficiently represent the actual cells in tissues, which are fully bounded by cells. As presented in Fig. 10(a) – (c), the trends corresponding to the primary geometrical parameters such as cell area, feret diameter and perimeter indicate that the model predictions are fairly in good agreement with both of the experimental findings. The shrinkage trends observed from these plots further indicate that the tissue model is superior to the single cell model, since the actual tissue scale effects such as intercellular contacts and middle lamella mechanisms were involved in the tissue model. However, the cell roundness trend as observed in Fig. 10(d) indicates some level of deviation from the experimental curves, which is due to the small-sized tissue model used for the simulations. Therefore, more

advanced tissue models with larger numbers of cells may be needed in order to minimize such model prediction discrepancies (Karunasena et al., 2014e). Next, as presented in Fig. 10(e), the tissue model predictions of cell elongation (EL) agree reasonably well with the gradually increasing EL trend of real tissues. The elongation increment indicates that the cells undergo irregular deformations during drying, where the major and minor axes lengths become different. Fig. 10(f) indicates some degree of over-prediction of the compactness trends, which can be explained similarly to the case of cell roundness by referring to the limited size of the tissue model used in this work.

4.3. Detailed analysis of morphological changes of potato tissues during drying

Fig. 11 presents the SEM images of potato tissues, which clearly indicate a closely-packed cellular structure which undergoes shrinkage during drying in the same manner as that of apple cells in tissues described in Section 4.1. By inspecting the SEM images for fresh cells, it can be confirmed that the potato cells are comparatively bigger than the apple cells, which agrees well with the cell diameter values used for the model (see Table 1). Also, the SEM images indicate some level of limited shrinkage of dried potato tissues compared to apple tissues, which agrees with the differences of the cell wall contraction effects discussed in Section 4.1. In the case of tissue simulations, Fig. 12 presents the overall view of the simulated potato tissues and Fig. 13 presents the corresponding enlarged views. As mentioned in Section 4.1, since the potato tissue is modelled with limited cell wall contraction effects, the overall tissue deformations are not very significant and the cells also have indicated a limited shrinkage, which agrees with the SEM images. Also, it is observed that the cell wall wrinkling effects in potato cells are almost negligible (see Fig. 13), which is due to the limited shrinkage characteristics of the cell wall. Compared to the constant pectin layer thickness used for the initial tissue setup (Fig. 13(a)), the pectin layer of fresh potato tissues has deformed unevenly along the cell circumference, which is mainly due to the highly-stretched cells walls in those turgid cells. In contrast, pectin layers of extremely dried tissue states (Fig. 13(e) and (f)) have relatively uniform thickness, which is due to the effect of lower turgor pressure and relaxed cell walls existing in dried tissues. Further, the larger cell size in potato tissue may also have some influence on the limited shrinkage behaviour and the limited cell wall wrinkling effects.

In the case of qualitative results, as presented in Fig. 14(a), the cell area predictions of the tissue model is in relatively good agreement with the gradually decreasing trend of the cell area observed from experimental findings (Campos-Mendiola et al., 2007). Further, the tissue simulation results indicate a better agreement than single cell model perditions, which can be explained in a similar way as discussed in Section 4.2. In the case of the cell feret diameter and the perimeter, a very good agreement is also observed when compared with the calculated values, which were evaluated based on the above mentioned experimental cell area trends. Further, the cell perimeter trends observed from Fig. 14(c) indicate that the single cell and tissue predictions are almost identical. This is because the perimeter reductions are basically governed by localized perimeter changes of the individual cells as defined in Eq. (A.8) and is minimally affected by intercellular influences. Next, in the case of cell roundness (Fig. 14(d)), the model indicates a gradually reducing trend, which compares well with the experimental trend (Lewicki and Pawlak, 2005). Finally, the cell elongation and compactness trends predicted by the tissue model as presented in Fig. 14(e) and (f) indicate a gradual increment in the elongation and gradual

decrement in the compactness. Here, due to the absence of any experimental curves for these two parameters, the curves can still be compared with the trends observed in the apple cells (Fig. 10(f)) and even with the single cell simulation results of potato. Firstly, when compared with the apple cells, the potato tissue results show similar EL and C trends, which represent the general irregular shrinking behaviour of plant tissues during drying. Also, compared to the single cell results, it is evident that the tissue simulation results have sufficiently captured the cellular shrinkage behaviour since the EL and C values have differed from the initial fresh cell values. On the other hand, single cells maintain quite unchanged EL and C values during drying, due to the absence of intercellular interactions.

4.4. Detailed analysis of morphological changes of carrot tissues during drying

Fig. 15 presents SEM images of carrot tissues at different moisture contents, obtained from drying experiments (Sansiribhan et al., 2012). From these SEM images, it is evident that the fresh carrot cells are fairly turgid and owns larger dimensions with clearly identifiable cell wall boundaries. During drying, the cells undergo a significant shrinkage, similar to the above mentioned apple and potato tissue behaviours. The shrinkage eventually results in highly wrinkled cell walls along with localized variation of cell shapes. These trends agree well with the tissue simulations presented in Fig. 16 and 17. A clear shrinking behaviour is observed where the cell and tissue dimensions reduce with significant localized cell shape differences within the tissue, which can be explained in a similar manner as discussed in Section 4.2 and 4.3. Further, as mentioned in Section 4.1, the inflated square shape observed from extremely dried carrot tissues as shown in Fig. 16(e) and (f) have resulted in localized differences of the cell shapes. The enlarged tissue views presented in Fig. 17 imply that the cell shape remains basically hexagonal even at the extensively dried tissue states, and the intense shrinkage behaviour results in localized cell wall wrinkling effects as observed from Fig. 17(f). Also the pectin layers of dried carrot tissues are much relaxed (Fig. 17(e) and (f)), than that in the case of turgid tissues (Fig. 17(b) - (d)).

In terms of quantitative cellular geometrical parameters, Fig. 18(a) – (c) indicate a good agreement between the model predictions and the experimental curves. Here, the cell diameter trends were directly obtained from experimental literature (Sansiribhan et al., 2010), and cell area and perimeter trends were deduced based on the cell diameter by assuming a circular 2D cell shape. Fig. 18(d) – (e) present the roundness, elongation and compactness variations and those trends follow the usual shrinking behavior observed in apple and potato tissues, which were explained above.

4.5. Detailed analysis of morphological changes of grape tissues during drying

In Fig. 19, grape tissue drying images obtained from Stereo microscopy are presented which correspond to the first stage of drying where the lowest moisture content attained during drying is limited to 0.6 X/X_0 (Ramos et al., 2004). The images generally indicate that the fresh cells are well attached to each other and are comparatively circular due to their turgid nature. As the tissues get dried, they undergo the typical shrinkage behaviour. However, the cell wall wrinkling effects are not clearly observed, which may be mainly due to the

lower magnification used in the original microscopy images. When considering the simulation results as presented in Fig. 20 and 21, the general shrinking behaviour is again observed, including the above mentioned localized cell shape differences and the bulk level tissue deformations. These simulations replicate the microscopy image based observations. Further, the enlarged tissue views as presented in Fig. 21 indicate some level of cell wall wrinkling behaviour, particularly in critically dried grape tissues (Fig. 21(e) and (f)).

Next, Fig. 22 presents the usual geometrical parameters corresponding to grape cells. The primary geometrical parameters such as cell area, feret diameter and perimeter indicate an acceptable agreement with the corresponding experimental curves, representing the general shrinking behaviour as discussed in Section 4.3. Also, in terms of secondary geometrical parameters such as cell roundness, elongation and compactness, the predictions are acceptable compared to the other food materials mentioned above.

5. Conclusion and outlook

A meshfree based 2-D microscale plant tissue model has been involved in this work in order to compare the morphological changes of different tissues (apple, potato, carrot and grapes) during drying. Cells in the tissues were modelled as hexagons and aggregated to form simplified tissues with customized properties corresponding to each plant food material. The models were simulated at different cell moisture contents and turgor pressure values in order to replicate different dryness states, and compared with experimental findings both qualitatively and quantitatively, which indicated a favourable agreement. When considering numerical studies conducted up to now in literature, this work is potentially the first study which focused on four distinct food material tissue simulations together, in order to study the comparative differences of morphological changes during drying. This work is further significant since a better-performing novel numerical technique was involved, compared to conventional grid-based techniques, which have previously demonstrated limited capability to account for complex mechanisms of dry plant food microstructure.

The simulation results indicated that, tissue morphological changes are mainly influenced by the cell size, wall thickness, wall stiffness, wall contractions, turgor pressure, and pectin layer dimensions and stiffness. Lager cell sizes or stiffer cell walls (higher cell wall Young's modulus or wall thickness) resist shrinkage during drying and produce relatively larger dried cells with minimum cell wall wrinkling. High turgor pressure negatively affects cellular shrinkage and produces inflated cell and tissue shapes with minimum local cell wall wrinkling. Pectin layer thickness and stiffness can also influence the localized morphological changes of tissues during drying.

The model has the flexibility to be further improved by incorporating bigger tissue with larger number of cells having heterogeneous shapes, intercellular spaces, and even extended to 3-D tissues. Further, the model can be upgraded to simulate localized variations of temperature, cell moisture content and turgor pressure, in order to mimic realistic phenomena such as case hardening. Also, these microscale deformation characteristics can be used to develop multiscale material models, which are highly useful in different simulation software packages to model material deformation during drying, which is currently not well developed. Even the proposed numerical

technique itself could be further developed as a reliable and standalone simulation tool for product and process improvements in food engineering. In this background, the significance of the proposed method is clearly evident.

6. Appendix A

6.1. Single cell model: DEM based cell wall model

As introduced in Section 2.1, the total force ($\boldsymbol{F_k}$) on any wall particle k can be derived as:

$$\boldsymbol{F}_k = \boldsymbol{F}^e_{kj} + \boldsymbol{F}^d_{kj} + \boldsymbol{F}^{rf}_{ki} + \boldsymbol{F}^{rw}_{kl} + \boldsymbol{F}^a_{ki} + \boldsymbol{F}^b_{kj} + \boldsymbol{F}^c_{kj}. \tag{A.1}$$

Here the $\boldsymbol{F}^e$ forces represent the cell wall resistance on extensions or contractions due to internal or external force interactions. Considering each wall element, a spring model is used to define the stiff forces $\boldsymbol{F}^e_{kj}$ on any wall particle k due to any bonded wall particle j as (Liedekerke et al., 2010):

$$\boldsymbol{F}^e_{kj} = GZ_0T_0\left(\lambda_\theta - \frac{1}{\alpha^2\lambda_\theta^5}\right), \tag{A.2}$$

where, G is the shear modulus ($\approx E/3$) with E being the Young's modulus of the wall material, Z_0 is the initial cell height, T_0 is the initial cell wall thickness, $\lambda_\theta = L/L_0$ is the extension ratio of any cell wall element at the current time step, L is the width of the wall element at the current time step (distance between particle k and j) and L_0 is its initial un-deformed width. The parameter α is calculated with β = 0.5 for cylindrical cells as follows (Liedekerke et al., 2010):

$$\alpha = \sqrt{\frac{\beta + \sqrt{\beta^2 - 4(\beta-1)/\lambda_\theta^6}}{2}}. \tag{A.3}$$

In Eq. A.1, $\boldsymbol{F}^d$ forces represent the viscous behaviour of the fibrous cell wall boundary and are defined by using a linear dashpot model. Therefore the viscous forces $\boldsymbol{F}^d_{kj}$ acting on any wall particle k due to the neighbouring wall particles j are calculated as (Liedekerke et al., 2010):

$$\boldsymbol{F}^d_{kj} = -\gamma\,\boldsymbol{v}_{kj}\,, \tag{A.4}$$

where, γ is the cell wall damping constant and $\boldsymbol{v}_{kj}$ is the velocity of particle k relative to particle j. The $\boldsymbol{F}^{rf}$, $\boldsymbol{F}^{rw}$ and $\boldsymbol{F}^a$ forces in Eq. (A.1) were used to define the wall-fluid interactions and boundary conditions. The repulsion forces $\boldsymbol{F}^{rf}_{ki}$ on any wall particle k from any other fluid particle i are defined as (Liedekerke et al., 2010; Liu and Liu, 2003):

$$\boldsymbol{F}^{rf}_{ki} = f^{rf}_{ki}\,\boldsymbol{x}_{ki}\,, \tag{A.5}$$

where, f^{rf}_{ki} is the magnitude of the repulsion force and $\boldsymbol{x}_{ki}$ is the position vector of particle k relative to particle i. The f^{rf}_{ki} is defined according to Lenard-Jones (LJ) force type as (Liedekerke et al., 2010):

$$f_{ki}^{rf} = \begin{cases} f_0^{rf}\left[\left(\frac{r_0}{r_{ki}}\right)^8 - \left(\frac{r_0}{r_{ki}}\right)^4\right]\left(\frac{1}{r_{ki}{}^2}\right) & \left(\frac{r_0}{r_{ki}}\right) \geq 1 \\ 0 & \left(\frac{r_0}{r_{ki}}\right) < 1\,, \end{cases} \tag{A.6}$$

where, r_0 is the initial gap between the two particles, r_{ki} is the current gap between them and f_0^{rf} is the strength of the LJ contact. Furthermore, in Eq. A.1, in order to avoid unphysical self-penetrations of the non-bonded wall-wall particles, a similar force interaction was used to define the repulsion forces $\boldsymbol{F}_{kl}^{rw}$ with an LJ contact strength of f_0^{rw}. Also the attraction forces $\boldsymbol{F}_{ki}^{a}$ were used to maintain fluid-wall contact during drying. Both interactions were modelled using LJ interactions with corresponding LJ contact strengths.

In Eq. A.1, a bending stiffness term ($\boldsymbol{F}_{kj}^{b}$) was used in order to account for the resistance that plant cell walls create when they experience local bending and wrinkling, and it was defined on any wall particle k within the k and j particle pair as (Karunasena et al., 2014b):

$$\boldsymbol{F}_{kj}^{b} = \frac{k_b}{L} tan\left(\frac{\Delta\theta}{2}\right), \tag{A.7}$$

where, k_b is the cell wall bending stiffness, L is the width of any given wall element at any given time step, θ is the external angle between the particular wall element and the adjacent wall element as shown in Fig. 2, and $\Delta\theta$ is the change of the θ angle during time evolution. Next, as given in Eq. A.1, in order to account for cell wall contractions during drying, cell wall contraction forces ($\boldsymbol{F}^{c}$) were used in the model and are defined as (Karunasena et al., 2014c):

$$\boldsymbol{F}_{kj}^{c} = k_{wc}\left[L - L_0'\left[1 - \frac{a}{b}\left(1 - \frac{X}{X_0}\right)\right]\right], \tag{A.8}$$

where, k_{wc} is the force coefficient of wall contractions, L is the current width of any particular wall element (see Fig. 1(d)), L_0' is the width of the wall element at fully turgid condition, a and b are empirical factors, and X/X_0 is the normalized moisture content of the dried cell to be simulated. The a and b were set by considering the normalized cell perimeter trends and the same k_{wc} was used for all food materials here (Karunasena et al., 2014c). Further, the cell wall drying effects were accounted by proportionally reducing the cell wall mass during drying (Karunasena et al., 2014c).

6.2. Single cell model: SPH based cell fluid model

The resultant force $\boldsymbol{F}_i$ on any fluid particle i was defined as:

$$\boldsymbol{F}_i = \boldsymbol{F}_{ii'}^{p} + \boldsymbol{F}_{ii'}^{v} + \boldsymbol{F}_{ik}^{rw} + \boldsymbol{F}_{ik}^{a}\,. \tag{A.9}$$

In Eq. (A.9), the pressure forces ($\boldsymbol{F}_{ii'}^{p}$) and viscous forces ($\boldsymbol{F}_{ii'}^{v}$) on any given fluid particle i are defined using the generic SPH fundamental formulations by involving the properties of the neighbouring fluid particles i' as (Liedekerke et al., 2010):

$$\boldsymbol{F}^{p}_{ii'} = -m_i \sum_{i'} m_{i'} \left(\frac{P_i}{\rho_i^2} + \frac{P_{i'}}{\rho_{i'}^2}\right)\left(\frac{1}{\mathrm{Z}}\right)\nabla_{\mathrm{i}} W_{ii'}, \tag{A.10}$$

542

$$\boldsymbol{F}^{v}_{ii'} = m_i \sum_{i'} \frac{m_{i'}(\mu_i + \mu_{i'})\boldsymbol{v}_{ii'}}{\rho_i \rho_{i'}}\left(\frac{1}{\mathrm{Z}}\right)\left(\frac{1}{r_{ii'}}\frac{\partial W_{ii'}}{\partial r_{ii'}}\right), \tag{A.11}$$

543 where at any given time, m, P, ρ, μ, Z and W are the particle mass, pressure, density, dynamic viscosity, cell
544 height and the smoothing kernel. For the smoothing kernel W, the quartic smoothing kernel was used for higher
545 accuracy and stability rather than the commonly used cubic spline kernel (Karunasena et al., 2012d). When
546 evaluating the W, the smoothing length was evolved in order to maintain approximately 20 particles within the
547 influencing domain (Karunasena et al., 2014b) :

$$h = \left(\frac{D}{D_0}\right) h_0 \,, \tag{A.12}$$

548 where, D is the average cell feret diameter at the current time step, D_0 is the initial cell diameter and h_0 is the
549 initial smoothing length (see Table 1 and Table 2). As the system evolves with time, the following equation is
550 used to update the fluid particle pressure as a function of slight fluid density variation (Liedekerke et al., 2010;
551 Liu and Liu, 2003):

$$P_i = P_T + K\left[\left(\frac{\rho_i}{\rho_0}\right)^7 - 1\right], \tag{A.13}$$

552 where, P_T is the uniquely set initial cell turgor pressure for each of the dried cell simulation (see Section 2.4.), K
553 is the fluid compression modulus, ρ_i is the current density of each fluid particle, and ρ_0 is its initial density
554 assumed to be equal to the density of water. Here, the K need to be set sufficiently higher in order to ensure the
555 fluid behaves in a fairly incompressible manner within the SPH scheme by minimizing large density
556 fluctuations. Next, the density of any fluid particle i is evolved using the following equation (Liedekerke et al.,
557 2010):

$$\frac{d\rho_i}{dt} = \frac{1}{Z}\frac{d\rho_i^*}{dt} - \frac{\rho_i^*}{Z^2}\frac{dZ}{dt} + \frac{\rho_i}{m_i}\frac{dm_i}{dt}. \tag{A.14}$$

558 The first term in Eq. (A.14) accounts for slight density changes of the cell fluid as the cell deforms in XY plane
559 and ρ_i^* is the 2-D density of any fluid particle i defined as $\rho_i^* = Z\rho_i$. Then the ρ_i^* fluctuations are defined using
560 the standard SPH continuity equation as:

$$\frac{d\rho_i^*}{dt} = m_i \sum_{i'} \boldsymbol{v}_{ii'} \cdot \nabla_{\mathrm{i}} W_{ii'} \,. \tag{A.15}$$

561 The second term in Eq. (A.14) adds a correction to the density evolution by compensating for any cell height
562 changes, and is defined as:

$$\frac{dZ}{dt} = \frac{Z_{t+\Delta t} - Z_t}{\Delta t}, \tag{A.16}$$

563 where, at any given time, $Z_{t+\Delta t}$ and Z_t are the cell heights at the current and previous time steps, and Δt is the
564 time step size. Here, the cell height is time evolved by considering the incompressibility of the cell wall material
565 as (Liedekerke et al., 2010):

$$Z = (\alpha\lambda_\theta)Z_0\,. \tag{A.17}$$

The third term in Eq. (A.14) accounts for the slight density changes within the SPH scheme as a result of the cell fluid mass transfer through the semi-permeable cell wall whenever there is a scalar difference between the cell fluid osmotic potential and the turgor pressure, and is defined as (Liedekerke et al., 2010; Taiz and Zeiger, 2010):

$$\frac{dm_i}{dt} = -\frac{A_c L_p \rho_i}{n_f}(P_i + \Pi)\,, \tag{A.18}$$

where A_c, L_p, n_f and Π represent total surface area of the cylindrical cell at any given time, cell wall permeability assumed to be uniform all over the cell surface, total number of fluid particles used to model the cell fluid and the osmotic potential of the cell fluid at a given dried cell state, respectively. The latter is carefully set to control the cell turgor pressure (Lewicki and Pawlak, 2003) because the amount of fluid transferred across the cell wall ceases when the value of P_i (> 0) becomes equal to the scalar value of Π.

The final two terms in Eq. (A.9) represent the fluid-wall boundary treatment which involves repulsion forces $\boldsymbol{F}_{ik}^{rw}$ and attraction forces $\boldsymbol{F}_{ik}^{a}$, and are defined in the same LJ force type as:

$$\boldsymbol{F}_{ik}^{rw} = \sum_k f_{ik}^{rw}\boldsymbol{x}_{ik}\,, \tag{A.19}$$

$$\boldsymbol{F}_{ik}^{a} = \sum_k f_{ik}^{a}\boldsymbol{x}_{ik}\,. \tag{A.20}$$

6.3. Tissue model

The pectin layer stiff force was defined as a linear spring model acting between the initially adjacent cell wall particles of any two adjacent cells, and defined as(Karunasena et al., 2014e):

$$\boldsymbol{F}_{km}^{e\_pectin} = -k_{pectin}\Delta\boldsymbol{x}_{km}\,, \tag{A.21}$$

where k_{pectin} is the pectin layer stiffness and $\Delta\boldsymbol{x}_{km}$ is the gap difference of the two particles compared to their initial gap. This force helps to maintain the gap between the wall particle pair equal to the initially set pectin layer thickness. Further, this is the only force acting in between cells if they try to separate each other beyond the initial pectin layer gap.

In case where the interacting cells become closer, pectin stiffness creates a repulsion force in order to separate the cells and thereby tries to return them back to their initial relative positions. The intensity of this force is usually insufficient to fully prevent the cells become very close and eventually interpenetrated. Therefore, a LJ type force is used for this purpose, and is defined as (Karunasena et al., 2014e):

$$\boldsymbol{F}_{km}^{rc} = \sum_j f_{km}^{rc}\boldsymbol{x}_{km}\,, \tag{A.22}$$

where, f_{km}^{rc} is the strength of the LJ force field and $\boldsymbol{x}_{km}$ is the position vector of particle k relative to particle m. Here, the f_{km}^{rc} is defined similar to that of the cell wall LJ force field.

7. Nomenclature

A	cell top surface area (m^2)
A_0	cell top surface area at fresh condition (m^2)
A/A_0	normalized cell area
A_c	total surface area of the cylindrical cell (m^2)
C	cell compactness
C_0	cell compactness at fresh condition
C/C_0	normalized cell compactness
D	cell feret diameter (m)
D_{major}	cell major axis length (m)
D_{minor}	cell minor axis length (m)
D_0	cell feret diameter at fresh condition (m)
D/D_0	normalized cell feret diameter
E	Young's modulus of the cell wall material (MPa)
EL	cell elongation
EL_0	cell elongation at fresh condition
EL/EL_0	normalized cell elongation
$\boldsymbol{F}^e$	cell wall stiff forces (N)
$\boldsymbol{F}^d$	cell wall damping forces (N)
$\boldsymbol{F}^{rf}$	wall-fluid repulsion forces (N)
$\boldsymbol{F}^{rw}$	wall-wall repulsion forces (N)
$\boldsymbol{F}^a$	wall-fluid attraction forces (N)
$\boldsymbol{F}^b$	forces due to the bending stiffness of the wall (N)
$\boldsymbol{F}^p$	cell fluid pressure forces (N)
$\boldsymbol{F}^v$	cell fluid viscous forces (N)
G	shear modulus of the cell wall material (MPa)
K	cell fluid compression modulus (MPa)
L	width of a given discrete wall element (m)
L'	width of a given discrete wall element at fully turgid state (m)
L_0	Initial width of a given discrete wall element (m)
L_p	cell wall permeability ($m^2\ N^{-1}\ s$)
P	cell perimeter (m)
P_0	cell perimeter at fresh condition (m)

P/P_0	normalized cell perimeter
P_a	pressure of any fluid particle *a* (Pa)
P_T	initial cell turgor pressure (Pa)
R	cell roundness
R_0	cell roundness at fresh condition
R/R_0	normalized cell roundness
S	ratio between fluid inter-particle distance and smoothing length (r_{ab}/h)
T	cell wall thickness (m)
T_0	initial cell wall thickness (m)
TP	positive cell turgor pressure effects
W	smoothing kernel
WD	cell wall contraction effects
WC	cell wall drying effects
X	x - coordinate axis
X	dry basis moisture content (kg $_{\text{water}}$/kg $_{\text{dry solid}}$)
X_0	dry basis moisture content at fresh condition
X/X_0	dry basis normalized moisture content
Y	y - coordinate axis
Z	cell height (m)
Z	z - coordinate axis
Z_0	initial cell height (m)
Z_t	cell height at the previous time step (m)
$Z_{t+\Delta t}$	cell height at the current time step (m)
f_0^{rf}	strength of the LJ repulsion forces between fluid and wall particles (N m^{-1})
f_0^{rw}	strength of the LJ repulsion forces between non-bonded wall particles (N m^{-1})
f_0^{a}	strength of the LJ attraction forces between fluid and wall particles (N m^{-1})
h	smoothing length (m)
h_0	initial smoothing length (m)
k_b	bending stiffness of cell wall material (N m rad^{-1})
k_{wc}	force coefficient of cell wall contractions (N m^{-1})
m_a	mass of any particle *a* (kg)
n_f	cell fluid particle number
n_w	cell wall particle number
r	cell radius (m)
r_{ab}	distance between any given particle *a* and *b* (m)
t	time (s)
$\boldsymbol{v}_{ab}$	velocity of any given particle *a* relative to any other particle *b* (m s^{-1})
$\boldsymbol{x}_{ab}$	position vector of any given particle *a* relative to any other particle *b* (m)

Δt	time step (s)
x_0	initial fluid grid spacing (m)
$\Delta\theta$	change of external angle θ of any given wall element (rad)
$\Delta \boldsymbol{x}_{ab}$	change of gap difference of any two particles *a* and *b* compared to their initial gap (m)
Π	osmotic potential of the cell (Pa)
α	factor governing the relationship between z-directional extension ratio and λ_θ of any wall element
β	parameter that relate 2-D deformations to 3-D deformations of any wall element
γ	cell wall damping constant (N m^{-1} s)
ε_0	initial minimum allowed gap between outer most fluid particles and cell wall partiles (m)
θ	external angle between any adjacent cell wall elements (rad)
λ_θ	extension ratio of any given cell wall element
μ_a	dynamic viscosity of any fluid particle *a* (Pa s)
ρ_a	density of any given fluid particle *a* (kg m^{-3})
ρ_0	initial density of the cell fluid (kg m^{-3})
ρ_a^*	2-D density of any given particle *a* ($\rho_a^* = Z\rho_a$) (kg m^{-2})

8. Acknowledgements

The authors acknowledge the support given by Queensland University of Technology (QUT) - Brisbane, Australia on behalf of the research facilities and High Performance Computing (HPC) facilities provided. The financial assistance provided by QUT, International Postgraduate Research Scholarship (IPRS), Australian Postgraduate Award (APA) scholarship, and ARC Future Fellowship Grant (FT100100172) are gratefully acknowledged. Also, we extend our special thanks to Dr. Inês N. Ramos and Prof. Cristina L.M. Silva of the Catholic University of Portugal for sharing their experimental data on grape tissue drying. Further, we extend our thanks to the graduate student Ms. Parva Hesami for the contributions in apple tissue drying experiments conducted at QUT. The authors also specially acknowledge the overall support provided by University of Ruhuna - Sri Lanka.

9. References

Bai, Y., Rahman, M.S., Perera, C.O., Smith, B., Melton, L.D., (2002). Structural Changes in Apple Rings during Convection Air-Drying with Controlled Temperature and Humidity. Journal of Agricultural and Food Chemistry 50(11), 3179-3185.

Bartlett, M.K., Scoffoni, C., Sack, L., (2012). The determinants of leaf turgor loss point and prediction of drought tolerance of species and biomes: a global meta-analysis. Ecology Letters 15(5), 393-405.

Campos-Mendiola, R., Hernández-Sánchez, H., Chanona-Pérez, J.J., Alamilla-Beltrán, L., Jiménez-Aparicio, A., Fito, P., Gutiérrez-López, G.F., (2007). Non-isotropic shrinkage and interfaces during convective drying of potato slabs within the frame of the systematic approach to food engineering systems (SAFES) methodology. Journal of Food Engineering 83(2), 285-292.

Colagrossi, A., Bouscasse, B., Antuono, M., Marrone, S., (2012). Particle packing algorithm for SPH schemes. Computer Physics Communications 183(8), 1641-1653.

Crapiste, G.H., Whitaker, S., Rotstein, E., (1988-a). Drying of cellular material—I. A mass transfer theory. Chemical Engineering Science 43(11), 2919-2928.

623 Fanta, S.W., Abera, M.K., Aregawi, W.A., Ho, Q.T., Verboven, P., Carmeliet, J., Nicolai, B.M., (2014).
624 Microscale modeling of coupled water transport and mechanical deformation of fruit tissue during
625 dehydration. Journal of Food Engineering 124(0), 86-96.
626 Frank, X., Perré, P., (2010). The Potential of Meshless Methods to Address Physical and Mechanical
627 Phenomena Involved during Drying at the Pore Level. Drying Technology 28(8), 932-943.
628 Funebo, T., Ahrné, L.l.a., Kidman, S., Langton, M., Skjöldebrand, C., (2000). Microwave heat treatment of
629 apple before air dehydration – effects on physical properties and microstructure. Journal of Food
630 Engineering 46(3), 173-182.
631 Gao, Q., Pitt, R.E., (1991). Mechanics of parenchyma tissue based on cell orientation and microstructure.
632 Transactions of the ASAE 34, 232-238.
633 Georget, D.M.R., Smith, A.C., Waldron, K.W., (2003). Modelling of carrot tissue as a fluid-filled foam. Journal
634 of Materials Science 38(9), 1933-1938.
635 Gingold, R.A., Monaghan, J.J., (1977). Smoothed particle hydrodynamics - Theory and application to non-
636 spherical stars. Monthly Notices of the Royal Astronomical Society 181, 375-389.
637 Grabowski, S., Marcotte, M., Ramaswamy, H.S., (2003). Drying of Fruits, Vegetables, and Spices in:
638 Chakraverty, A., Mujumdar, A.S., Raghavan, G.S.V., Rawaswamy, H. (Eds.), *Handbook of postharvest*
639 *technology : cereals, fruits, vegetables, tea, and spices*. Marcel Dekker, New York pp. 653-695.
640 Han, Q.-H., Yin, L.-J., Li, S.-J., Yang, B.-N., Ma, J.-W., (2010). Optimization of Process Parameters for
641 Microwave Vacuum Drying of Apple Slices Using Response Surface Method. Drying Technology 28(4),
642 523-532.
643 Hepworth, D.G., Bruce, D.M., (2000). Measuring the Deformation of Cells within a Piece of Compressed Potato
644 Tuber Tissue. Annals of Botany 86(2), 287-292.
645 Hiller, S., Bruce, D.M., Jeronimidis, G., (1996). A micro-penetration technique for mechanical testing of plant
646 cell walls. Journal of Texture Studies 27(5), 559-587.
647 Hills, B.P., Remigereau, B., (1997). NMR studies of changes in subcellular water compartmentation in
648 parenchyma apple tissue during drying and freezing. International Journal of Food Science & Technology
649 32(1), 51-61.
650 Honda, H., Tanemura, M., Nagai, T., (2004). A three-dimensional vertex dynamics cell model of space-filling
651 polyhedra simulating cell behavior in a cell aggregate. Journal of Theoretical Biology 226(4), 439-453.
652 Jangam, S.V., (2011). An Overview of Recent Developments and Some R&D Challenges Related to Drying of
653 Foods. Drying Technology 29(12), 1343-1357.
654 Jeong, S., Park, S.-H., Kim, C.-H., (2013). Simulation of Morphology Changes in Drying Leaves. Computer
655 Graphics Forum 32(1), 204-215.
656 Karunasena, H.C.P., Hesami, P., Senadeera, W., Gu, Y.T., Brown, R.J., Oloyede, A., (2014a). Scanning
657 Electron Microscopic Study of Microstructure of Gala Apples During Hot Air Drying. Drying Technology
658 32(4), 455-468.
659 Karunasena, H.C.P., Senadeera, W., Brown, R.J., Gu, Y.T., (2014c). Simulation of plant cell shrinkage during
660 drying – A SPH–DEM approach. Engineering Analysis with Boundary Elements 44(0), 1-18.
661 Karunasena, H.C.P., Senadeera, W., Brown, R.J., Gu, Y.T., (2014e). A Particle Based Model to Simulate
662 Microscale Morphological Changes of Plant Tissues during Drying. Soft Matter 10(29), 5249-5268.
663 Karunasena, H.C.P., Senadeera, W., Gu, Y.T., Brown, R.J., (2012d). A Coupled SPH-DEM Model for Fluid and
664 Solid Mechanics of Apple Parenchyma Cells During Drying, in: Brandner, P.A., Pearce, B.W. (Eds.), *18th*
665 *Australian Fluid Mechanics Conference*. Australasian Fluid Mechanics Society, Launceston - Australia.
666 Karunasena, H.C.P., Senadeera, W., Gu, Y.T., Brown, R.J., (2014b). A Coupled SPH-DEM Model for Micro-
667 scale Structural Deformations of Plant Cells during Drying. Applied Mathematical Modelling 38(15-16),
668 3781-3801.
669 Karunasena, H.C.P., Senadeera, W., Gu, Y.T., Brown, R.J., (2014d). A Meshfree Model for Plant Tissue
670 Deformations during Drying. ANZIAM Journal 55 (EMAC2013), C110-C137.
671 Lee, C.Y., Salunkhe, D.K., Nury, F.S., (1967). Some chemical and histological changes in dehydrated apple.
672 Journal of the Science of Food and Agriculture 18(3), 89-93.
673 Lewicki, P.P., Drzewucka, J., (1998). Effect of drying on tissue structure of selected fruits and vegetables, in:
674 Mujumdar, A.S., akritidis, C.B., Marinos-Kouris, D., Saravacos, G.D. (Eds.), *Proceedings of the 11th*
675 *International Drying Symposium Drying 98*. Ziti Editions Thessaloniki, Greece, pp. 1093-1099.
676 Lewicki, P.P., Pawlak, G., (2003). Effect of Drying on Microstructure of Plant Tissue. Drying Technology
677 21(4), 657-683.
678 Lewicki, P.P., Pawlak, G., (2005). Effect of Mode of Drying on Microstructure of Potato. Drying Technology
679 23(4), 847-869.

Liedekerke, P.V., Ghysels, P., Tijskens, E., Samaey, G., Smeedts, B., Roose, D., Ramon, H., (2010). A particle-based model to simulate the micromechanics of single-plant parenchyma cells and aggregates. Physical Biology 7(2), 026006.
Liu, G.R., Liu, M.B., (2003). *Smoothed Particle Hydrodynamics : A Meshfree Particle Method*. World Scientific Publishing Co., Singapore.
Liu, Z., Hong, W., Suo, Z., Swaddiwudhipong, S., Zhang, Y., (2010). Modeling and simulation of buckling of polymeric membrane thin film gel. Computational Materials Science 49(1, Supplement), S60-S64.
Lozano, J.E., Rotstein, E., Urbicain, M.J., (1980). Total porosity and open-pore porosity in the drying of fruits. Journal of Food Science 45(5), 1403-1407.
Martin, O., Osvaldo, C., Ganesan, N., Rakesh, S., Weitnauer, A., (2006). Food Dehydration, in: Dennis, R.H., Lund, D.B. (Eds.), *Handbook of Food Engineering, Second Edition*. CRC Press, pp. 601-744.
Mayor, L., Sereno, A.M., (2004). Modelling shrinkage during convective drying of food materials: a review. Journal of Food Engineering 61(3), 373-386.
Mayor, L., Silva, M.A., Sereno, A.M., (2005). Microstructural Changes during Drying of Apple Slices. Drying Technology 23(9-11), 2261-2276.
McGarry, A., (1993). Influence of Water Status on Carrot (Daucus Carota L.) Fracture Properties. Journal of Horticultural Science & Biotechnology 68(3), 431-438.
McGarry, A., (1995). Cellular Basis of Tissue Toughness in Carrot (Daucus carota L.) Storage Roots. Annals of Botany 75(2), 157-163.
Rahman, M.S., Al-Zakwani, I., Guizani, N., (2005). Pore formation in apple during air-drying as a function of temperature: porosity and pore-size distribution. Journal of the Science of Food and Agriculture 85(6), 979-989.
Ramos, I.N., Silva, C.L.M., Sereno, A.M., Aguilera, J.M., (2004). Quantification of microstructural changes during first stage air drying of grape tissue. Journal of Food Engineering 62(2), 159-164.
Ramos, M.I.F.N., (2010). Integrated Approach on Field Solar Drying, Pilot Convective Drying and Microstructural Changes, *School of Biotechnology*. Catholic University of Portugal Porto - Portugal.
Rudge, T., Haseloff, J., (2005). A Computational Model of Cellular Morphogenesis in Plants, in: Capcarrère, M., Freitas, A., Bentley, P., Johnson, C., Timmis, J. (Eds.), *Advances in Artificial Life*. Springer Berlin Heidelberg, pp. 78-87.
Sabarez, H.T., Gallego-Juarez, J.A., Riera, E., (2012). Ultrasonic-Assisted Convective Drying of Apple Slices. Drying Technology 30(9), 989-997.
Sansiribhan, S., Devahastin, S., Soponronnarit, S., (2010). Quantitative Evaluation of Microstructural Changes and their Relations with Some Physical Characteristics of Food during Drying. Journal of Food Science 75(7), E453-E461.
Sansiribhan, S., Devahastin, S., Soponronnarit, S., (2012). Generalized microstructural change and structure-quality indicators of a food product undergoing different drying methods and conditions. Journal of Food Engineering 109(1), 148-154.
Schlosser, J., Olsson, N., Weis, M., Reid, K., Peng, F., Lund, S., Bowen, P., (2008). Cellular expansion and gene expression in the developing grape (Vitis vinifera L.). Protoplasma 232(3-4), 255-265.
Stukowski, A., (2010). Visualization and analysis of atomistic simulation data with OVITO–the Open Visualization Tool. Modelling and Simulation in Materials Science and Engineering 18(1), 015012.
Taiz, L., Zeiger, E., (2010). Water and Plant Cells, *Plant Physiology*. Sinauer Associates, Sunderland, USA, pp. 73-84.
Van Liedekerke, P., Ghysels, P., Tijskens, E., Samaey, G., Roose, D., Ramon, H., (2011). Mechanisms of soft cellular tissue bruising. A particle based simulation approach. Soft Matter 7(7), 3580-3591.
Wang, C.X., Wang, L., Thomas, C.R., (2004). Modelling the Mechanical Properties of Single Suspension-Cultured Tomato Cells. Annals of Botany 93(4), 443-453.
Witrowa-Rajchert, D., Rząca, M., (2009). Effect of Drying Method on the Microstructure and Physical Properties of Dried Apples. Drying Technology 27(7-8), 903-909.
Wu, N., Pitts, M.J., (1999). Development and validation of a finite element model of an apple fruit cell. Postharvest Biology and Technology 16(1), 1-8.
Zhu, H.X., Melrose, J.R., (2003). A Mechanics Model for the Compression of Plant and Vegetative Tissues. Journal of Theoretical Biology 221(1), 89-101.

10. Figures and tables

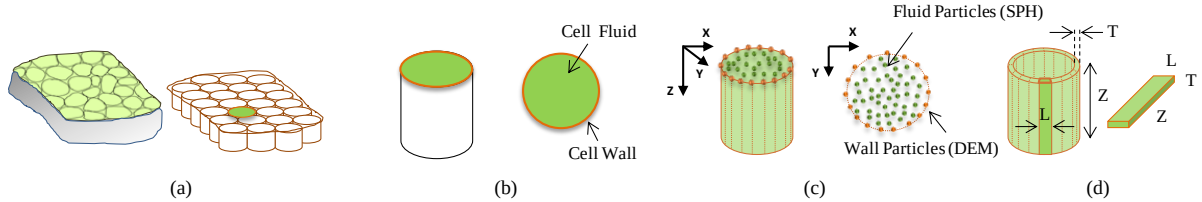

Fig.1. (a) A plant tissue simply represented as an aggregate of cylindrical cells, (b) 2-D model to represent any cylindrical cell; (c) particle scheme used for the 2-D Cell model: fluid model based on SPH particles and wall model based on DEM particles; and (d) discrete elements of the cell wall.

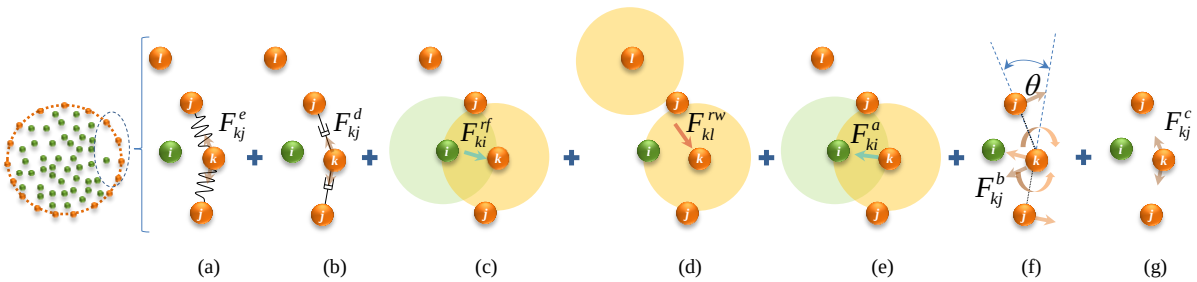

Fig. 2. Force interactions used in the DEM-based cell wall model: wall stiff forces ($\boldsymbol{F}^{e}_{kj}$), wall damping forces ($\boldsymbol{F}^{d}_{kj}$), wall-fluid repulsion forces ($\boldsymbol{F}^{rf}_{ki}$), non-bonded wall-wall repulsion forces ($\boldsymbol{F}^{rw}_{kl}$), wall-fluid attraction forces ($\boldsymbol{F}^{a}_{ki}$), forces due to wall bending stiffness ($\boldsymbol{F}^{b}_{kj}$), and forces for cell wall contractions during drying ($\boldsymbol{F}^{c}_{kj}$). (i : fluid particles; j, k & l : wall particles)

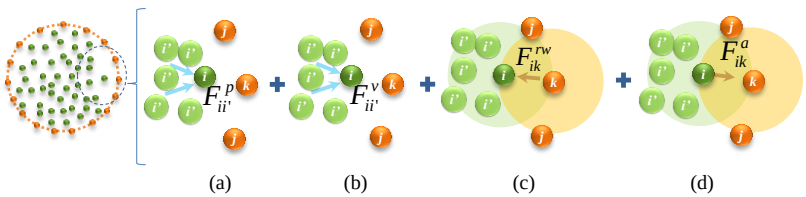

Fig. 3. Force interactions used in the SPH based cell fluid model: pressure force ($\boldsymbol{F}^{p}_{ii'}$), viscous force ($\boldsymbol{F}^{v}_{ii'}$), wall-fluid repulsion forces ($\boldsymbol{F}^{rw}_{ik}$), and wall-fluid attraction forces ($\boldsymbol{F}^{a}_{ik}$). (i & i' : fluid particles; j & k: wall particles)

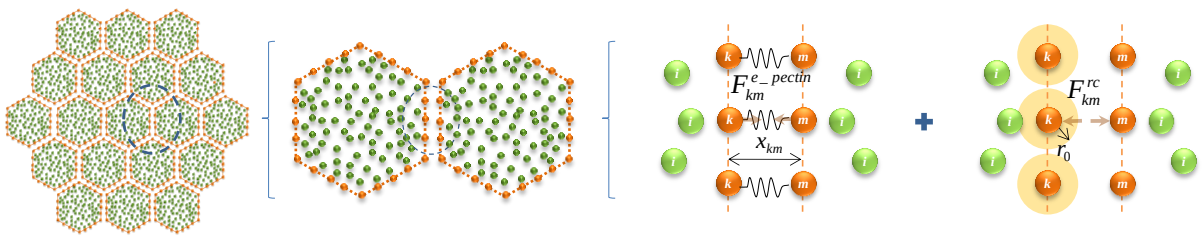

Fig. 4. Tissue model and cell-cell force interactions: (a) hexagonal shaped cells are used for tissue initialization with positive pectin layer gap; (b) interacting wall particle pairs of adjacent cells; (c) pectin layer stiff forces ($\boldsymbol{F}^{e\_pectin}_{km}$); and (d) cell-cell repulsion forces ($\boldsymbol{F}^{rc}_{km}$). (i: fluid particles; k & m: wall particles)

Table 1 Customized model parameters for different plant materials

Parameter	Food variety used for modelling			
	Apple	Potato	Carrot	Grape
	Value (Source)	Value (Source)	Value (Source)	Value (Source)
Initial cell diameter (D_0)	150 µm (Karunasena et al., 2014a)	200 µm (Hepworth and Bruce, 2000; Lewicki and Pawlak, 2005)	100 µm (Lewicki and Drzewucka, 1998; McGarry, 1995; Sansiribhan et al., 2010)	150 µm (Schlosser et al., 2008)
Initial cell height (Z_0)	100 µm (= 2/3 D_0)	133 µm (= 2/3 D_0)	53 µm (= 2/3 D_0)	100 µm (= 2/3 D_0)
Wall initial thickness (T_0)	6 µm (Liedekerke et al., 2010; Wu and Pitts, 1999)	1 µm (Hepworth and Bruce, 2000)	2 µm (Georget et al., 2003; McGarry, 1995)	3 µm (Schlosser et al., 2008)
Pectin layer thickness (T_p)	8 µm (set)	10 µm (set)	4 µm (set)	8 µm (set)
Pectin layer stiffness (k_{pectin})	20 N m^{-1} (set)	20 N m^{-1} (set)	10 N m^{-1} (set)	20 N m^{-1} (set)
Wall shear modulus ($G \approx E/3$)	18 MPa (Liedekerke et al., 2010; Wu and Pitts, 1999)	166 MPa (Hepworth and Bruce, 2000; Hiller et al., 1996)	33 MPa (set)	33 MPa (set)
Empirical factors on cell wall contraction (a, b)	0.2, 0.9 (Karunasena et al., 2014a)	0.07, 0.92 (Campos-Mendiola et al., 2007)	0.36, 0.93 (Sansiribhan et al., 2010)	0.18, 0.43 (Ramos, 2010)
Fresh cell turgor pressure (P_T)	200 kPa (Liedekerke et al., 2010)	200 kPa (set)	400 kPa (McGarry, 1993)	200 kPa (set)
Fresh cell osmotic potential (Π)	-200 kPa (= $-P_T$)	-200 kPa (= $-P_T$)	-400 kPa (= $-P_T$)	-200 kPa (= $-P_T$)

Table 2 Generally used model parameters for all plant materials

Parameter	Value	Source
Fluid viscosity (μ)	0.1 Pa s	set (Liedekerke et al., 2010)
Initial fluid density (ρ_0)	1000 kg m^{-3}	set (Liedekerke et al., 2010)
Wall permeability (L_P)	2.5 × 10^{-6} m^2 N^{-1} s	set (Karunasena et al., 2014b)
Wall bending stiffness (k_b)	1 × 10^{-12} N m rad^{-1}	set (Karunasena et al., 2014e)
Wall damping ratio (γ)	5 × 10^{-6} N m^{-1} s	set (Karunasena et al., 2014b)
Fluid compression modulus (K)	20 MPa	set (Karunasena et al., 2014b)
Wall contraction force coefficient (k_{wc})	4 × 10^{4} N m^{-1}	set (Karunasena et al., 2014e)
LJ contact strength for wall-fluid repulsions (f_0^{rf})	1 × 10^{-12} N m^{-1}	set (Karunasena et al., 2014e)
LJ contact strength for wall-wall repulsions (f_0^{rw})	1 × 10^{-12} N m^{-1}	set (Karunasena et al., 2014e)
LJ contact strength for wall-fluid attractions (f_0^{a})	2 × 10^{-12} N m^{-1}	set (Karunasena et al., 2014e)
LJ contact strength for cell-cell repulsions (f_0^{rc})	1 × 10^{-10} N m^{-1}	set (Karunasena et al., 2014e)
Initial smoothing length (h_0)	1.2 × initial fluid grid spacing	set (Karunasena et al., 2014e)
Time step (Δt)	2 × 10^{-9} s	set (Karunasena et al., 2014e)

Table 3 Literature data used for qualitative and quantitative model validation

Plant variety	Qualitative data (microscopy images)	Quantitative data					
		A	D	P	R	EL	C
Apple	(Karunasena et al., 2014a)	(Karunasena et al., 2014a)					
Potato	Our experiments	(Campos-Mendiola et al., 2007)			(Lewicki and Pawlak, 2005)	-	-
Carrot	(Sansiribhan et al., 2012)	(Sansiribhan et al., 2010)			-	-	-
Grapes	(Ramos et al., 2004)	(Ramos et al., 2004; Ramos, 2010)					

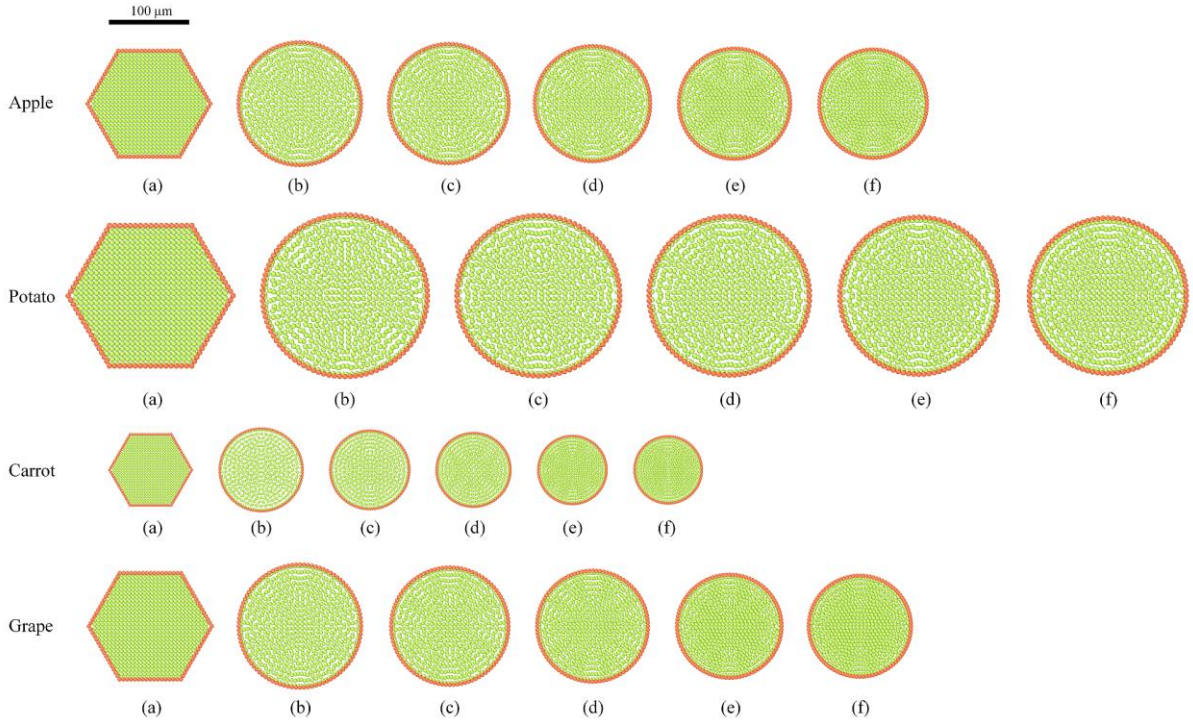

Fig. 5. Single cell simulations at different states of dryness: (a) initial condition before simulations, (b) X/X_0= 1.0, (c) X/X_0 = 0.8, (d) X/X_0 = 0.6, (e) X/X_0 = 0.4, and (f) X/X_0 = 0.25.

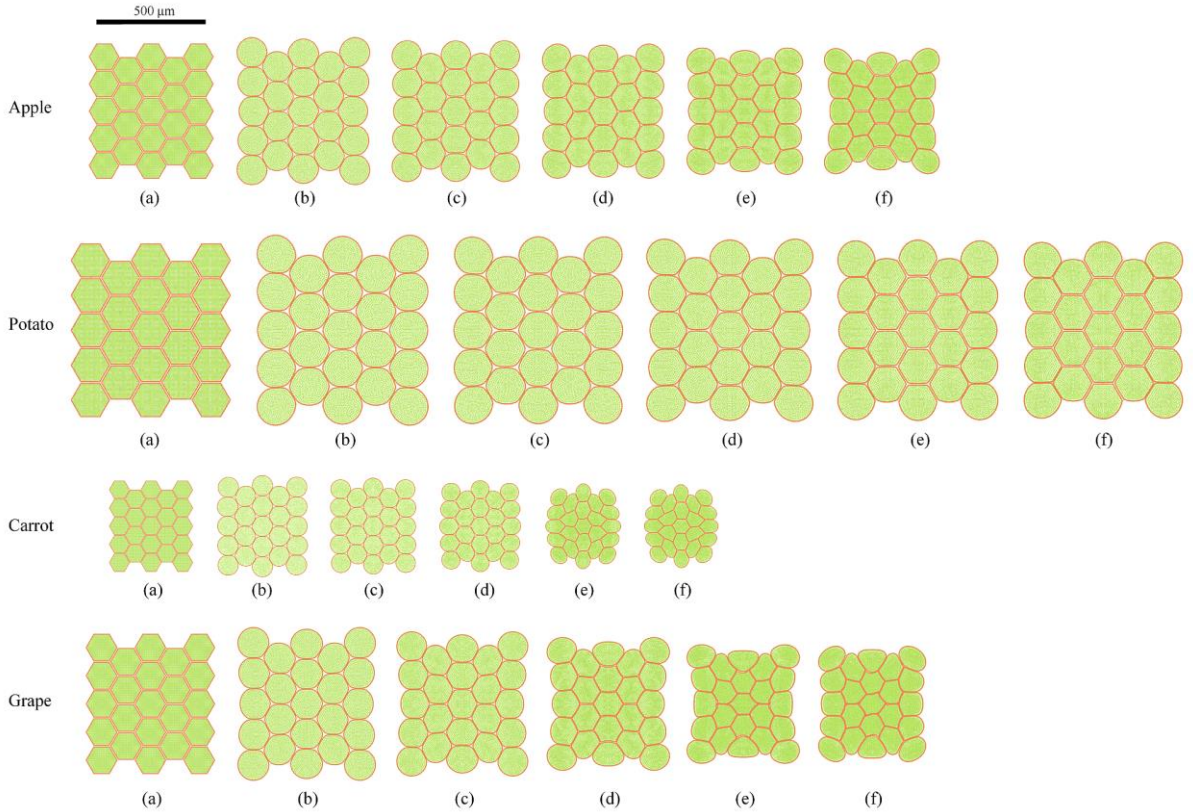

Fig. 6. Tissue simulations at different states of dryness: (a) initial condition before simulations, (b) X/X_0= 1.0, (c) X/X_0 = 0.8, (d) X/X_0 = 0.6, (e) X/X_0 = 0.4, and (f) X/X_0 = 0.25.

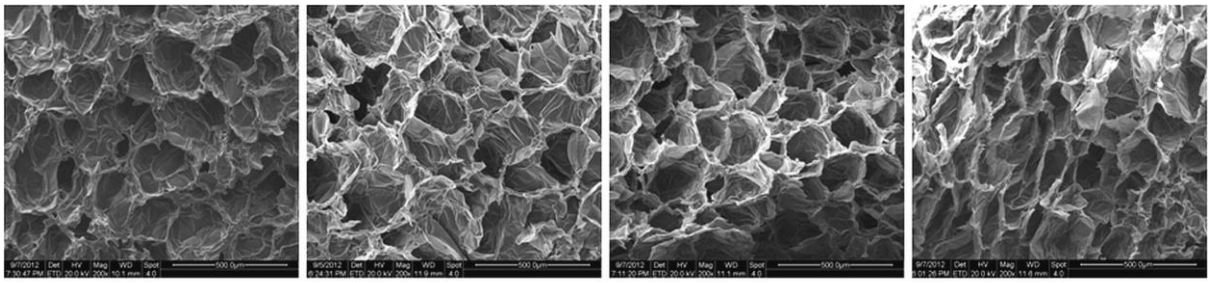

(a) (b) (c) (d)

Fig. 7. Scanning Electron Microscopy (SEM) images of apple tissues at different states of dryness: (a) X/X_0= 1.0, (b) X/X_0 = 0.5, (c) X/X_0 = 0.2, and (d) X/X_0 = 0.1. (bar is 500 μm)

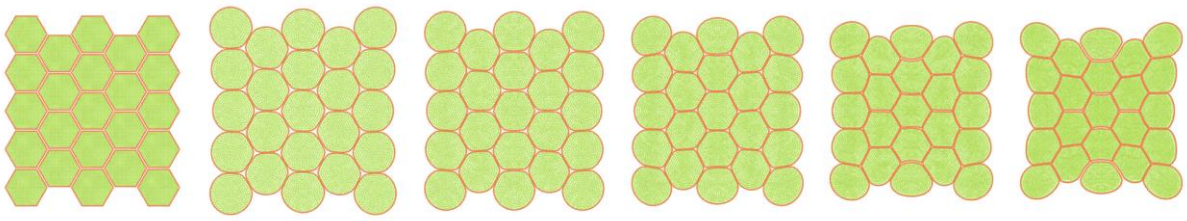

(a) (b) (c) (d) (e) (f)

Fig. 8. Apple tissue simulations at different states of dryness: (a) initial condition before simulations, (b) X/X_0= 1.0, (c) X/X_0 = 0.8, (d) X/X_0 = 0.6, (e) X/X_0 = 0.4, and (f) X/X_0 = 0.25.

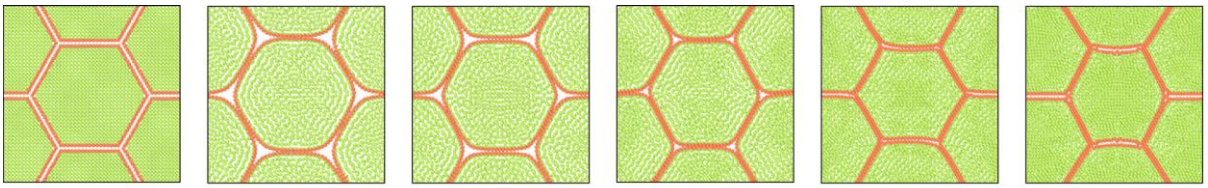

(a) (b) (c) (d) (e) (f)

Fig. 9. Apple tissue simulations at different states of dryness (enlarged view): (a) initial condition before simulations, (b) X/X_0= 1.0, (c) X/X_0 = 0.8, (d) X/X_0 = 0.6, (e) X/X_0 = 0.4, and (f) X/X_0 = 0.25.

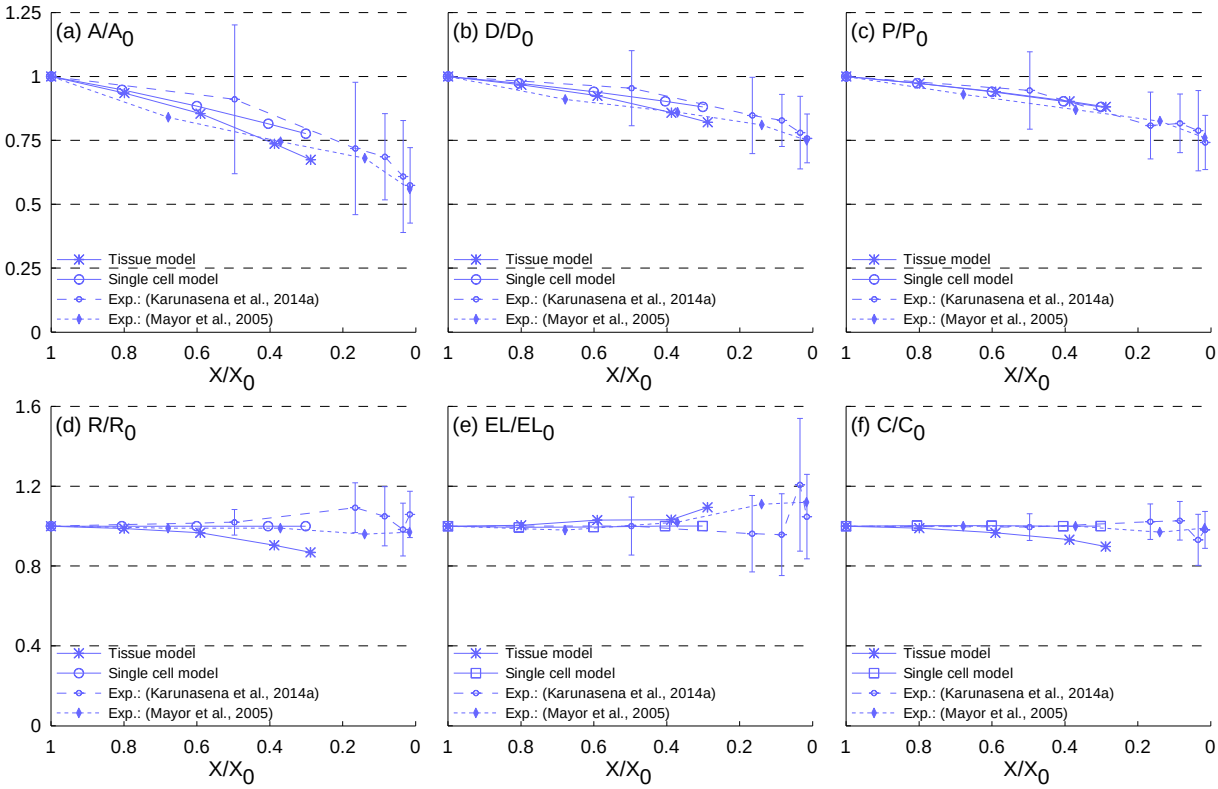

Fig. 10. Influence of drying for cellular geometrical parameter variations of apple tissues: (a) A/A_0, (b) D/D_0, (c) P/P_0, (d) R/R_0, (e) EL/EL_0, and (f) C/C_0. (Error bars indicate one standard deviation)

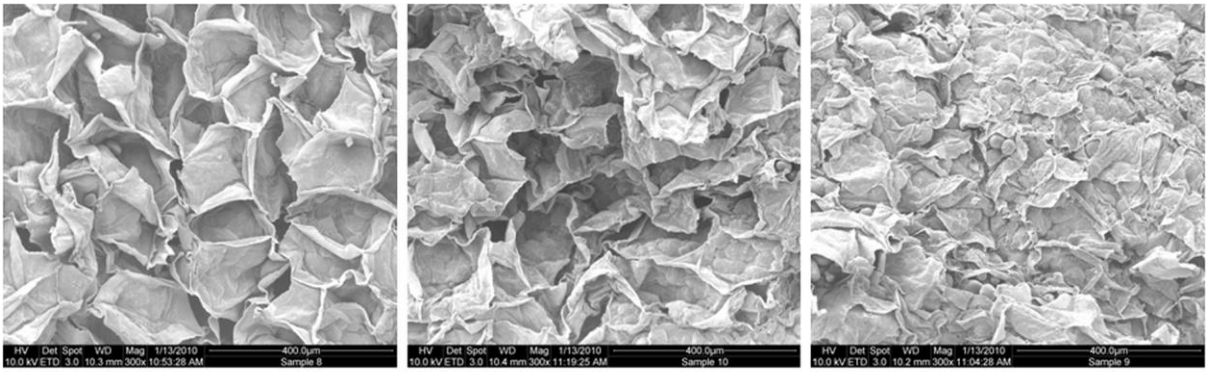

Fig. 11. SEM images of potato tissues at different states of dryness: (a) X/X_0= 1.0, (b) X/X_0 = 0.5, and (c) X/X_0 = 0.3. (bar is 400 µm)

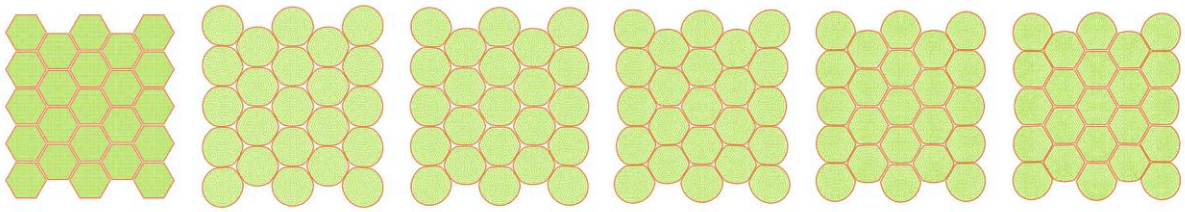

Fig. 12. Potato tissue simulations at different states of dryness: (a) initial condition before simulations, (b) X/X_0= 1.0, (c) X/X_0 = 0.8, (d) X/X_0 = 0.6, (e) X/X_0 = 0.4, and (f) X/X_0 = 0.25.

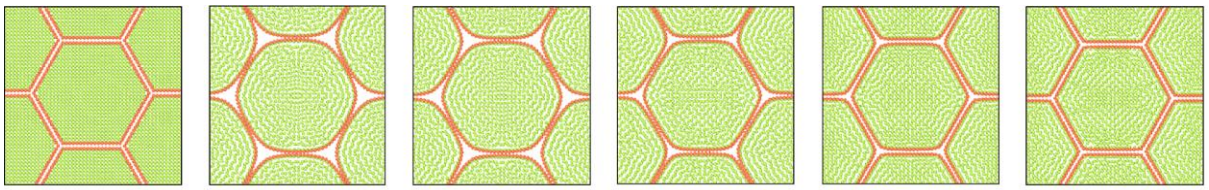

Fig. 13. Potato tissue simulations at different states of dryness (enlarged view): (a) initial condition before simulations, (b) X/X_0= 1.0, (c) X/X_0 = 0.8, (d) X/X_0 = 0.6, (e) X/X_0 = 0.4, and (f) X/X_0 = 0.25.

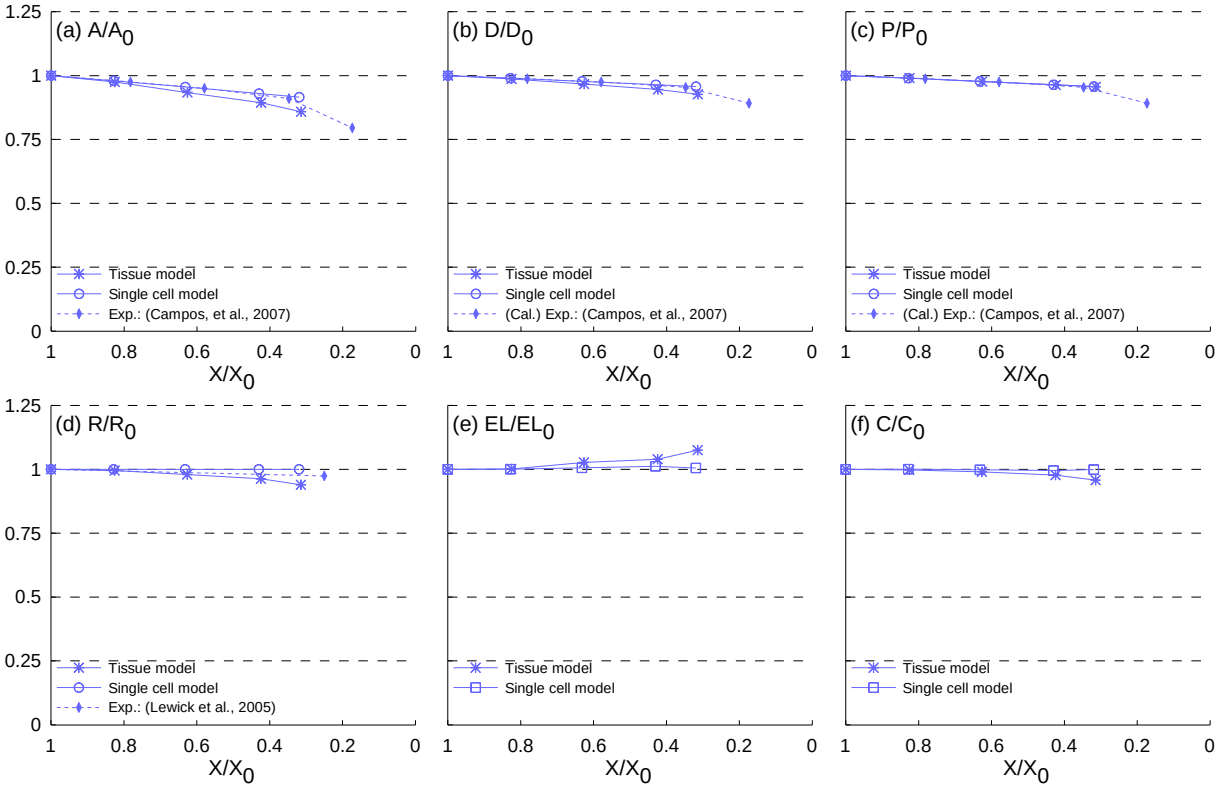

Fig. 14. Influence of drying for cellular geometrical parameter variations of potato tissues: (a) A/A_0, (b) D/D_0, (c) P/P_0, (d) R/R_0, (e) EL/EL_0, and (f) C/C_0.

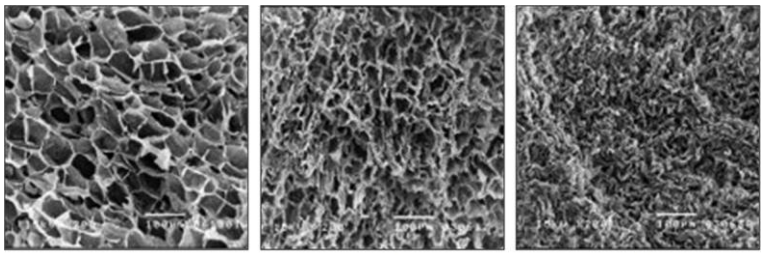

Fig. 15. SEM images of carrot tissues at different states of dryness[5]: (a) X/X_0= 1.0, (b) X/X_0 = 0.27, and (c) X/X_0 = 0.01. (bar is 100 μm)

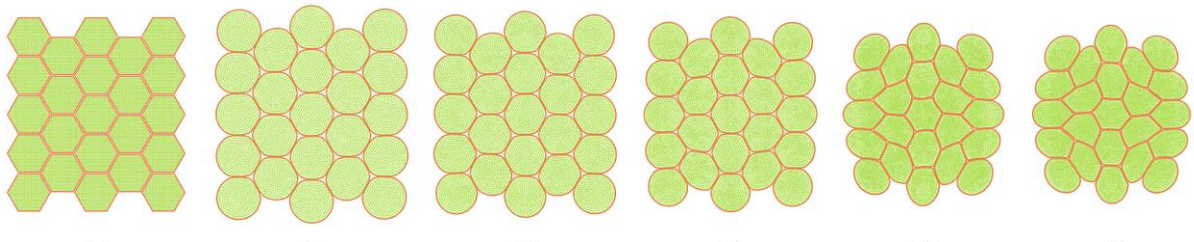

Fig. 16. Carrot tissue simulations at different states of dryness: (a) initial condition before simulations, (b) X/X_0= 1.0, (c) X/X_0 = 0.8, (d) X/X_0 = 0.6, (e) X/X_0 = 0.4, and (f) X/X_0 = 0.25.

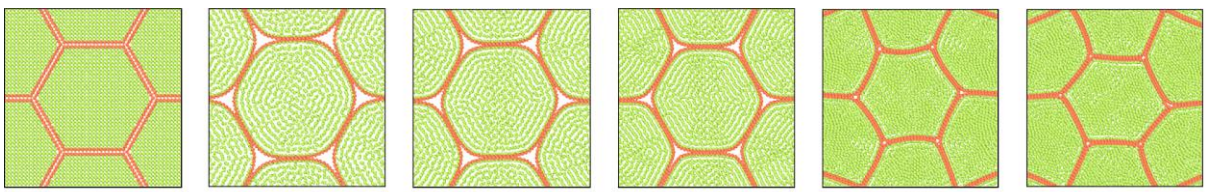

Fig. 17. Carrot tissue simulations at different states of dryness (enlarged view): (a) initial condition before simulations, (b) X/X_0= 1.0, (c) X/X_0 = 0.8, (d) X/X_0 = 0.6, (e) X/X_0 = 0.4, and (f) X/X_0 = 0.25.

[5] "Reprinted from Journal of Food Engineering, 109(1), Sansanee Sansiribhan, Sakamon Devahastin and Somchart Soponronnarit, Generalized microstructural change and structure-quality indicators of a food product undergoing different drying methods and conditions, 148-154, Copyright (2012), with permission from Elsevier"

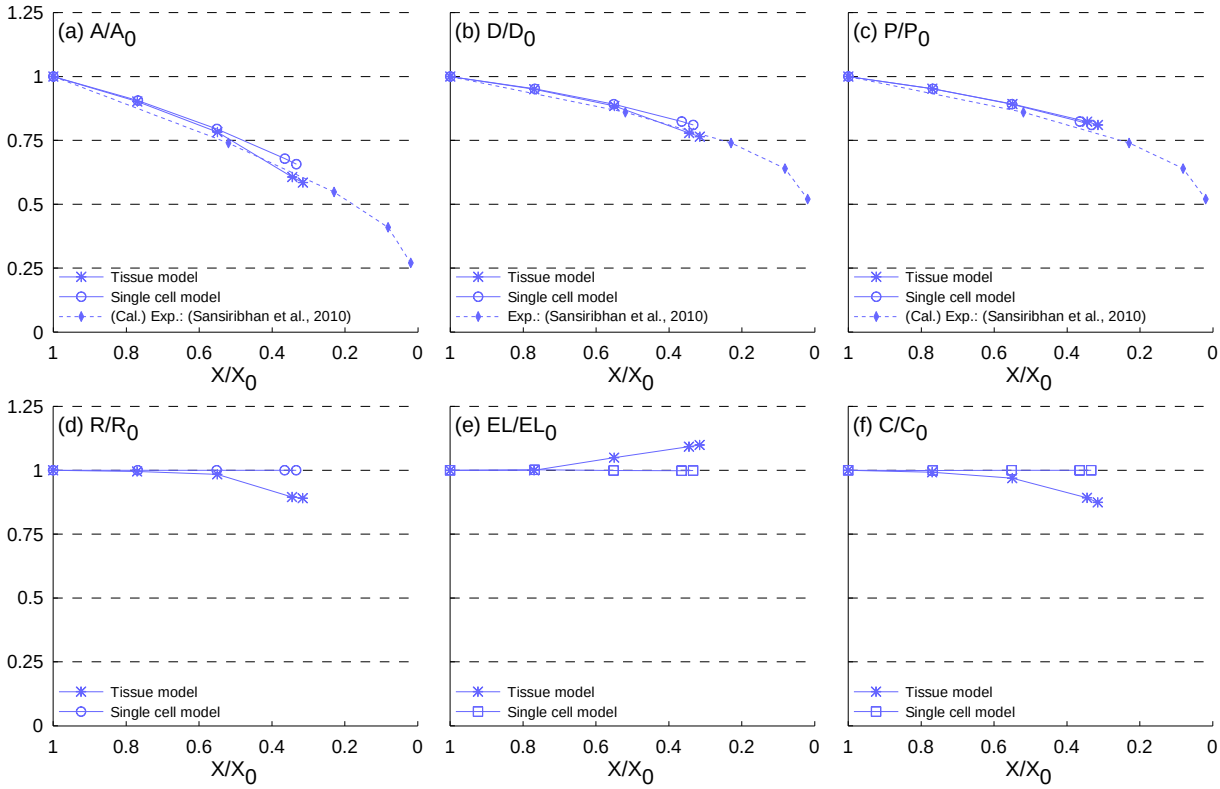

Fig. 18. Influence of drying for cellular geometrical parameter variations of carrot tissues: (a) A/A_0, (b) D/D_0, (c) P/P_0, (d) R/R_0, (e) EL/EL_0, and (f) C/C_0.

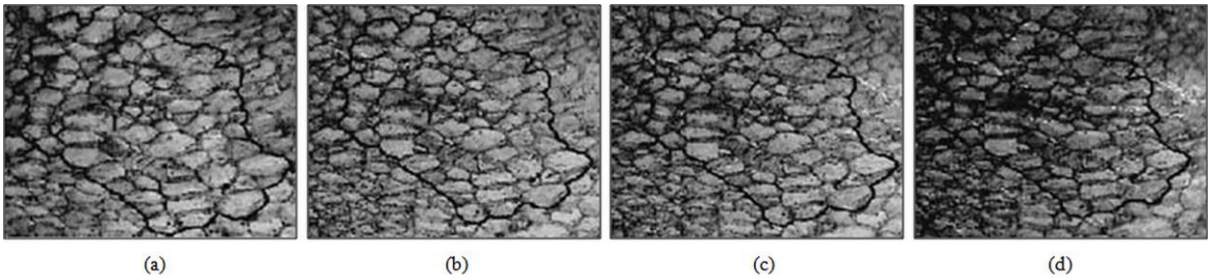

Fig. 19. Stereo microscopy images of grape tissues at different states of dryness[6]: (a) X/X_0= 1.0, (b) X/X_0 = 0.71, (c) X/X_0 = 0.66, and (d) X/X_0 = 0.58.

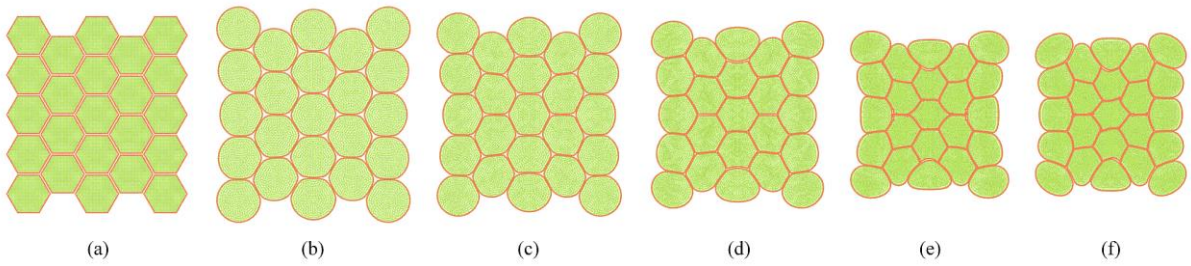

Fig. 20. Grape tissue simulations at different states of dryness: (a) initial condition before simulations, (b) X/X_0= 1.0, (c) X/X_0 = 0.8, (d) X/X_0 = 0.6, (e) X/X_0 = 0.4, and (f) X/X_0 = 0.25.

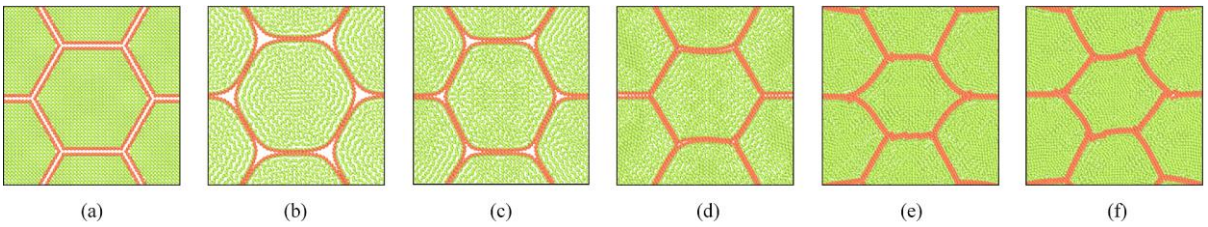

Fig. 21. Grape tissue simulations at different states of dryness (enlarged view): (a) initial condition before simulations, (b) X/X_0= 1.0, (c) X/X_0 = 0.8, (d) X/X_0 = 0.6, (e) X/X_0 = 0.4, and (f) X/X_0 = 0.25.

[6] "Reprinted from Journal of Food Engineering, 62(2), Inês N. Ramos, Cristina L.M. Silva, Alberto M. Sereno and José M. Aguilera, Quantification of microstructural changes during first stage air drying of grape tissue, 159-164, Copyright (2004), with permission from Elsevier"

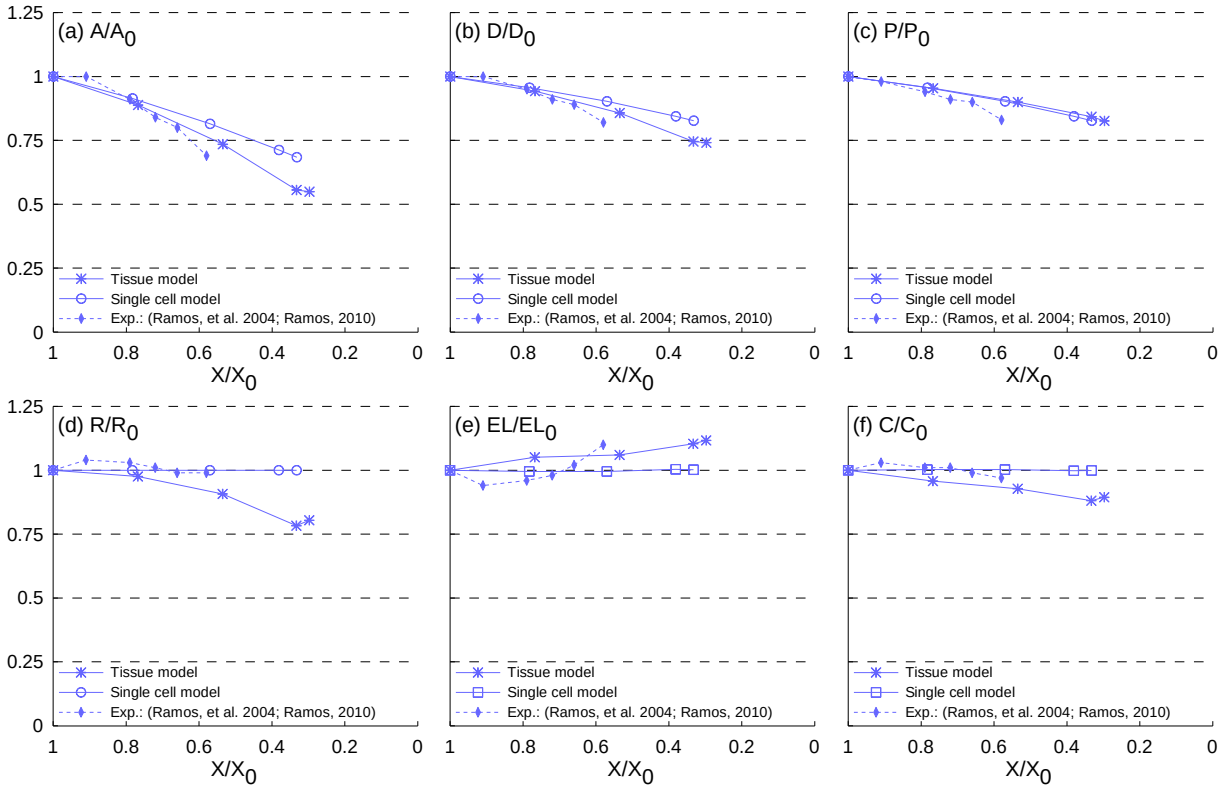

Fig. 22. Influence of drying for cellular geometrical parameter variations of grape tissues: (a) A/A_0, (b) D/D_0, (c) P/P_0, (d) R/R_0, (e) EL/EL_0, and (f) C/C_0.